

# An oncohistone-driven H3.3K27M/CREB5/ID1 axis maintains the stemness and malignancy of diffuse intrinsic pontine glioma

Received: 12 June 2024

Accepted: 2 April 2025

Published online: 17 April 2025

 Check for updates

Wei Zhou<sup>1,7</sup>, Cheng Xu<sup>2,7</sup>, Shuangrui Yang<sup>1</sup>, Haocheng Li<sup>1</sup>, Changcun Pan<sup>2</sup>, Zhuang Jiang<sup>2</sup>, Luyang Xie<sup>2</sup>, Xiaohan Li<sup>3</sup>, Huimin Qiao<sup>3</sup>, Da Mi<sup>3</sup>, Yujie Tang<sup>4</sup>, Liwei Zhang<sup>2,5</sup> ✉ & Qiaoran Xi<sup>1,6</sup> ✉

Diffuse intrinsic pontine glioma (DIPG), a lethal pediatric cancer driven by H3K27M oncohistones, exhibits aberrant epigenetic regulation and stem-like cell states. Here, we uncover an axis involving H3.3K27M oncohistones, CREB5/ID1, which sustains the stem-like state of DIPG cells, promoting malignancy. We demonstrate that CREB5 mediates elevated ID1 levels in the H3.3K27M/ACVR1WT subtype, promoting tumor growth; while BMP signaling regulates this process in the H3.1K27M/ACVR1MUT subtype. Furthermore, we reveal that H3.3K27M directly enhances *CREB5* expression by reshaping the H3K27me3 landscape at the *CREB5* locus, particularly at super-enhancer regions. Additionally, we elucidate the collaboration between CREB5 and BRG1, the SWI/SNF chromatin remodeling complex catalytic subunit, in driving oncogenic transcriptional changes in H3.3K27M DIPG. Intriguingly, disrupting *CREB5* super-enhancers with ABBV-075 significantly reduces its expression and inhibits H3.3K27M DIPG tumor growth. Combined treatment with ABBV-075 and a BRG1 inhibitor presents a promising therapeutic strategy for clinical translation in H3.3K27M DIPG treatment.

Diffuse intrinsic pontine glioma (DIPG), a subset of diffuse midline glioma (DMG), is an aggressive and devastating malignant tumor that mainly affects the pediatric population. This lethal brainstem tumor is characterized by a grim median survival period of approximately 10 months<sup>1–5</sup>. Genomic investigations have unveiled prevalent mutations in histone H3, where lysine 27 is replaced with methionine (K27M), found in about 80% of DIPG cases (i.e., 60% H3.3K27M and 20%

H3.1K27M DIPG). These mutations are often referred to as oncohistones due to their role as driver mutations in the tumorigenesis of DIPG<sup>6–12</sup>.

The main impact of H3K27M mutations limits the spreading of H3K27me3 repressive marks by affecting the enzymatic activity of PRC2, especially the conversion of di- to tri-methylation of H3K27, thereby preventing lateral spreading to neighboring nucleosomes,

<sup>1</sup>MOE Key Laboratory of Protein Sciences, State Key Laboratory of Molecular Oncology, School of Life Sciences, Tsinghua University, Beijing, China.

<sup>2</sup>Department of Neurosurgery, Beijing Tiantan Hospital, Capital Medical University, Beijing, China. <sup>3</sup>State Key Laboratory of Membrane Biology, Tsinghua-Peking Center for Life Sciences, IDG/McGovern Institute for Brain Research, School of Life Sciences, Tsinghua University, Beijing, China. <sup>4</sup>Key Laboratory of Cell Differentiation and Apoptosis of National Ministry of Education, Shanghai Key Laboratory of Reproductive Medicine, Department of Histoembryology, Genetics and Developmental Biology, Shanghai Jiao Tong University School of Medicine, Shanghai, China. <sup>5</sup>China National Clinical Research Center for Neurological Diseases, Beijing, China. <sup>6</sup>Joint Graduate Program of Peking-Tsinghua-NIBS, Tsinghua University, Beijing, China. <sup>7</sup>These authors contributed equally: Wei Zhou, Cheng Xu. ✉e-mail: [zhanglw@bjtt.org](mailto:zhanglw@bjtt.org); [xiqiaoran@mail.tsinghua.edu.cn](mailto:xiqiaoran@mail.tsinghua.edu.cn)

rather than influencing the recruitment of PRC2 or the deposition of H3K27me1/me2<sup>8,11–22</sup>. Studies on chromatin in H3K27M-glioma samples have revealed altered enhancer profiles associated with oncohistone variants and their context, resulting in abnormal gene expression<sup>23,24</sup>. This dysregulation leads to the stalling of DIPG cells in a cancer stem cell-like oligodendrocyte precursor cell (OPC)-like state that is capable of self-renewal and tumor initiation<sup>25,26</sup>. Although a few DIPG tumor cells still differentiate toward astrocytic-like (AC-like) and oligodendrocytic-like (OC-like) cell states, only OPC-like tumor cells are able to produce tumor xenografts in mice, suggesting an inverse relationship between differentiation and tumorigenicity<sup>25,27</sup>. This implies that oncohistone-driven epigenetic activation may awaken oncogenic transcription factors that are essential for the tumorigenesis of DIPG, potentially enhancing stemness and malignancy.

CREB5, a transcription factor known for its high affinity for cAMP-response elements (CREs), distinguishes itself from other CREB family members by lacking a homologous PKA-regulated activating phosphorylation site, making it non-responsive to the cAMP/PKA signaling pathway<sup>28–30</sup>. CREB5 plays roles in mouse embryonic development<sup>31,32</sup>, immune responses<sup>33</sup>, and neuroplasticity<sup>34,35</sup>. However, its dysregulation can lead to developmental defects or diseases, such as cancer<sup>30</sup>. CREB5 is frequently overexpressed or amplified in multiple cancers<sup>29,30,36</sup>. The mechanism by which CREB5 functions as an oncogenic transcription factor remains to be elucidated.

Proteins known as ID (inhibitor of DNA binding) inhibit differentiation and promote stemness by sequestering differentiation-associated transcription factors<sup>37–41</sup>. They are highly expressed in stem and progenitor cells and low in differentiated cells<sup>42</sup>. ID proteins are frequently deregulated in many types of human neoplasms, endowing cancer cells with stemness, cell proliferation, and multipotency features<sup>43,44</sup>. ID1, a downstream target of BMP (bone morphogenetic protein) signaling, is often upregulated in H3.1K27M DIPG due to the high activity of BMP signaling<sup>42,45–51</sup>. However, in H3.3K27M DIPG which has low BMP signaling activity<sup>52</sup>, ID1 overexpression persists, indicating an alternative regulatory pathway<sup>48</sup>. The mechanism by which H3.3K27M oncohistones influence ID1 expression in H3.3K27M DIPG remains unresolved.

Here, we show an oncohistone-driven CREB5/ID1 axis that connects oncohistone-induced epigenetic activation to oncogenic transcription factors in H3.3K27M DIPG, thereby promoting stemness and malignancy. We find that *Creb5* is specifically overexpressed in forebrain progenitor cells but remains silenced in hindbrain progenitor cells, the repression that is reversed upon H3.3K27M introduction. Moreover, H3.3K27M oncohistones prime CREB5 expression by reprogramming the H3K27me3 landscape at the CREB5 locus, a process facilitated by super-enhancer promoter interactions. Mechanistically, we demonstrate that CREB5 cooperates with BRG1 to regulate the malignant transcriptional program of DIPG. Finally, we show that targeting the CREB5 super-enhancer with ABBV-075 significantly reduces CREB5 expression and inhibits H3.3K27M DIPG tumor growth. The combined treatment with ABBV-075 and a BRG1 inhibitor offers a potential therapeutic strategy for H3.3K27M DIPG.

## Results

### ID1 functions as an oncogenic factor by promoting proliferation and stemness in H3K27M DIPG

ID1 often endows cancer cells with stemness and malignancy hijacked from normal stem cells<sup>43,44</sup> and its high expression in DIPG patients has a reduced survival time<sup>53</sup>. ID1 is upregulated in H3.1K27M DIPG due to the high activity of BMP signaling and functions as an oncogenic factor<sup>42,45–51</sup>. We first examined whether ID1 is highly expressed in H3.3K27M DIPG patients and cells. Immunohistochemistry (IHC) analysis demonstrated a significantly higher number of ID1-positive cells in the tumors of H3.3K27M DIPG patients compared to the pons of non-DIPG patients (Fig. 1a and Supplementary Table 1). Immunoblotting

showed that ID1 levels were significantly higher in three DIPG patient-derived cell lines including both H3.3K27M (DIPG17 and TT150630) and H3.1K27M/ACVR1mutant (DIPG-IV) DIPG cells than in pontine progenitor cells (PPCs<sup>52,54</sup>), the normal control cells (Fig. 1b and Supplementary Table 1). Thus, ID1 is significantly highly expressed in both H3.3K27M and H3.1K27M DIPG.

Next, we investigated whether ID1 functions as an oncogenic factor to promote stemness and malignancy of H3.3K27M DIPG by examining the cell proliferation and stemness in both ID1 knockdown (KD) and shRNA-scramble control DIPG cells (Supplementary Fig. 1a). The extent of proliferation was significantly reduced in ID1-KD cells compared to control cells (Supplementary Fig. 1b). And qPCR results showed that ID1 knock-down led to the downregulation of stemness/OPC-like progenitor markers (*SOX2* and *OLIG2*)<sup>52,55</sup> (Supplementary Fig. 1c). These findings support the role of ID1 in promoting cell proliferation and maintaining the stemness.

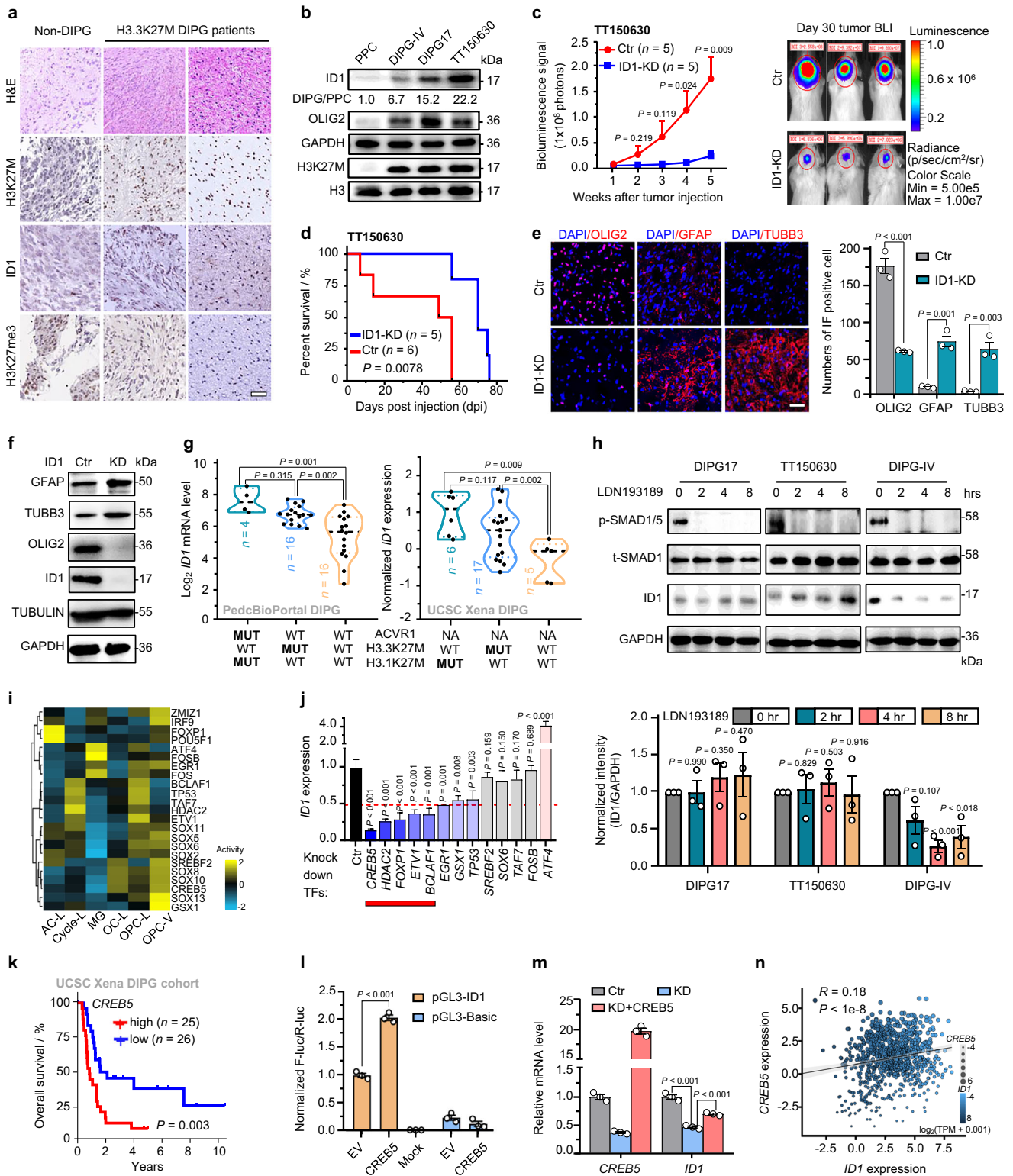
We then examined the impact of ID1 KD in two xenograft models (inoculation of ID1 KD or scramble control stable TT150630 cells and DIPG17 cells). The ID1-KD groups showed significant reductions in tumor size and significantly longer survival time than the control groups (Fig. 1c, d and Supplementary Fig. 1d). Moreover, in assessing the therapeutic potential of ID1, we injected adeno-associated virus (AAV) containing shRNAs targeting ID1 into DIPG17 xenograft mice. The AAV-ID1-KD groups demonstrated significant inhibition of tumor growth and prolonged survival compared to the control AAV group (Supplementary Fig. 1e, f). Hematoxylin and eosin (H&E) staining of tumor regions revealed ID1 KD mice had markedly lower numbers of tumor cells compared with control (Supplementary Fig. 1g). Beyond proliferation, we also examined stemness and differentiation markers with immunofluorescence (IF) staining of tumor sections and immunoblotting assay: we detected a significant decrease in the level of OLIG2 and significant increases in the levels of two differentiation markers (GFAP and TUBB3)<sup>4,27</sup> in ID1-KD tumors compared to controls (Fig. 1e, f and Supplementary Fig. 1h), establishing that disrupting ID1 reduces the stemness and promotes differentiation in DIPG.

These results support ID1's oncogenic impacts, including promoting tumor growth and maintaining H3K27M DIPG stemness.

### CREB5 regulates ID1 expression independently of the BMP signaling pathway in H3.3K27M DIPG

Considering the low activity of BMP signaling in H3.3K27M DIPG<sup>52</sup>, we next examined whether the ID1 transcription regulation is independent of BMP signaling in this subtype. We assessed two clinical DIPG cohorts (PedsBioPortal and UCSC Xena). We detected significantly elevated ID1 expression levels in H3.3K27M/ACVR1WT and H3.1K27M/ACVR1MUT DIPG subtypes as compared to the H3 WT DIPG subtype (Fig. 1g and Supplementary Data 1), consistent with aforementioned results (Fig. 1a, b). We explored the role of BMP signaling in the regulation of ID1 expression in H3.1K27M/ACVR1 mutant DIPG cells by employing isogenic cells with SMAD1 KD. Western blot analysis of DIPG-IV cells with and without SMAD1 KD, confirmed that SMAD1 depletion significantly reduces ID1 expression (Supplementary Fig. 1i), which supports the critical role of BMP signaling in regulating ID1 expression in these cells.

We then used LDNI93189, a specific inhibitor targeting ALK2/3 (aka ACVR1/BMPR-1A)<sup>42,45–51</sup>, to inhibit BMP signaling activation. Immunoblotting assays showed that blocking BMP signaling with LDNI93189 at indicated time course can drastically inhibit ID1 expression in DIPG-IV (H3.1K27M/ACVR1MUT) cells (Fig. 1h). In contrast, ID1 protein levels remained unchanged in TT150630 and DIPG17 (H3.3K27M/ACVR1WT) cells after LDNI93189 treatment in different time points (Fig. 1h), supporting the involvement of other regulators, independent of BMP signaling, in ID1 regulation in H3.3K27M DIPG cells.



To identify regulators contributing to the observed increased expression of *ID1* in the malignant H3.3K27M DIPG cells, we conducted SCENIC analysis<sup>56,57</sup> of public DIPG scRNA-seq data<sup>25</sup>. We identified 23 transcription factors (TFs) expressed at aberrantly high levels in malignant OPC-like cells compared to other more differentiated cells (AC- or OC-like cells) (Fig. 1i and Supplementary Fig. 2a). We then excluded 11 candidate TFs that appeared to be regulated by *ID1*, as evidenced by qPCR results comparing ID1-KD with the scramble control (Supplementary Fig. 2b) and conducted a small-scale shRNA

screen in DIPG17 cells targeting the remaining 12 TFs (Supplementary Fig. 2c). Knockdown of 5/12 of these TFs (*CREB5*, *HDAC2*, *FOXPI*, *ETV1*, and *BCLAF1*) significantly reduced *ID1* expression (Fig. 1j and Supplementary Fig. 2d).

We then conducted Kaplan-Meier analysis for subgroups defined for these five candidates (median expression as the cutoff) from two clinical DIPG cohorts<sup>58,59</sup> and found that the subgroups exhibiting higher expression levels of *CREB5* and *FOXPI* correlate with significantly poorer survival outcomes in DIPG patients (Fig. 1k and

**Fig. 1 | CREB5 regulates *ID1* expression independently of the BMP signaling pathway in H3.3K27M DIPG.** **a** H&E-stained sections or immunohistochemistry for H3K27M, *ID1*, and H3K27me3 in human non-DIPG pontine and DIPG samples. Scale bar: 50  $\mu$ m. **b** Immunoblotting analysis of the indicated proteins in PPCs, the H3.1K27M DIPG cells (DIPG-IV), and the H3.3K27M DIPG cells (DIPG17 and TT150630). **c** The bioluminescence activity (left) and representative bioluminescence images (BLI) (right) in TT150630 mouse models between *ID1* KD and Ctr ( $n = 5$ ). **d** Kaplan-Meier survival analysis from animals implanted with TT150630 cells with or without *ID1* KD in the pons. **e** Immunofluorescence images of pons sections from TT150630 PDX animals with or without *ID1* KD for anti-OLIG2, anti-GFAP, and anti- $\beta$ -tubulin with quantification. Scale bar: 20  $\mu$ m. Right panel: quantified cell counts. **f** Immunoblotting analysis of indicated proteins in DIPG17 cells with or without *ID1* KD. **g** *ID1* expression across indicated DIPG subtypes from PedsBioPortal and UCSC Xena DIPG cohort. **h**, Immunoblotting analysis (top) and quantification (bottom) of *ID1* expression in indicated DIPG cells treated with LDN-

193189 (200 nM) for 0, 2, 4, and 8 hours. **i** Clustering heatmap showing regulon specificities in OPC-like cells. **j** qPCR analysis of *ID1* expression in indicated DIPG cells. **k** Kaplan-Meier survival curves for DIPG patients from UCSC Xena cohort separated into *CREB5* high and low expression groups. **l**, Dual-luciferase reporter assay using *ID1* promoter. **m** qPCR analysis of *CREB5* and *ID1* in indicated DIPG cells. **n** Scatter plot showing the correlation of *ID1* and *CREB5* expression in clinical pediatric brain tumors (CBTTC). The  $p$  value and correlation coefficient ( $R$ ) were calculated using Pearson's correlation. The error bands indicate 95% CIs as shades based on standard error. Data presented as mean  $\pm$  s.e.m. of three independent experiments (**e**, **j**, **l**, and **m**) or mean  $\pm$  s.e.m. (**c**); statistical significance was determined by a two-tailed unpaired Student's  $t$ -test (**c**, **e**, **j**, **l**, **m**, and **n**), log-rank test (**d** and **k**) or ordinary one-way ANOVA with Tukey test (**g** and **h**). Experiments were repeated three times independently with similar results (**b**, **f** and **h**). Source data are provided as a Source Data file.

Supplementary Fig. 2e). To determine if either of these genes directly regulate *ID1* transcription in H3.3K27M DIPG, we constructed a dual-luciferase reporter system using the *ID1* promoter (Supplementary Fig. 2f) and measured the luciferase activity in DIPG17 cells transiently transfected with *CREB5* or *FOXPI*. The luciferase activity was significantly elevated in *CREB5*-transfected cells (Fig. 1l); no difference was observed in cells transfected with *FOXPI* (Supplementary Fig. 2g). Hence, *CREB5* serves as an upstream positive regulator of *ID1* expression.

We also found that *CREB5* overexpression in *CREB5*-KD DIPG17 cells (by transient transfection) partially restored *ID1* expression (Fig. 1m). Additionally, we identified a positive correlation between *ID1* expression levels and *CREB5* levels in the clinical pediatric brain tumor atlas (CBTTC cohort,  $R = 0.18$ ) (Fig. 1n). Note that we detected the presence of a short *CREB5* isoform in clinical pediatric brain tumors (CBTTC cohort) (Supplementary Fig. 2h); however, we found no differences in prognosis or regulation of *ID1* expression for this short isoform (Supplementary Fig. 2i, j).

These findings suggest that BMP signaling, constitutively activated by the *ACVR1* mutation, positively regulates *ID1* transcription in the H3.1K27M DIPG subtype, whereas *CREB5* exerts a positive regulatory effect on *ID1* transcription in the H3.3K27M DIPG subtype, independently of the BMP signaling pathway.

### CREB5 maintains an OPC/stem-like state and promotes tumor growth of H3.3K27M DIPG

Given that *CREB5* promotes *ID1* transcription in H3.3K27M DIPG, we next examined the expression of *CREB5* in this subtype DIPG. qPCR analysis revealed significantly higher expression of *CREB5* in H3.3K27M DIPG cells than in normal PPC cells and in DIPG-IV (H3.1K27M subtype) cells (Supplementary Fig. 3a). Moreover, public RNA-seq data from two cohorts of DIPG patient tumors<sup>38,60</sup> showed that the *CREB5* expression in H3.3K27M DIPG tumors was significantly higher than in pairwise normal tissues (Fig. 2a); H3.3K27M DIPG tumors also have significantly higher *CREB5* levels compared to H3.1K27M/H3WT DIPG tumors (Fig. 2b). This significantly elevated expression of *CREB5* in H3.3K27M DIPGs alongside the aforementioned link between increased *CREB5* expression and poorer prognosis in H3.3K27M DIPG (Fig. 1k and Supplementary Fig. 3b, c) together suggest that *CREB5* functions as an oncogenic factor in H3.3K27M DIPG.

Having established that *ID1* promotes proliferation and stemness downstream of *CREB5*, we next sought to determine whether *CREB5* itself promotes proliferation and stemness in H3.3K27M DIPG. We then conducted cell viability and neurosphere formation assays examining DIPG17 and TT150630 cells and detected significantly reduced cell proliferation for the *CREB5*-KD cell groups compared to controls (Fig. 2c, d and Supplementary Fig. 3d). Limiting dilution assay indicated a significant inhibition of cancer stemness in *CREB5*-KD DIPG cells compared to the scramble controls (Fig. 2e). Moreover, flow

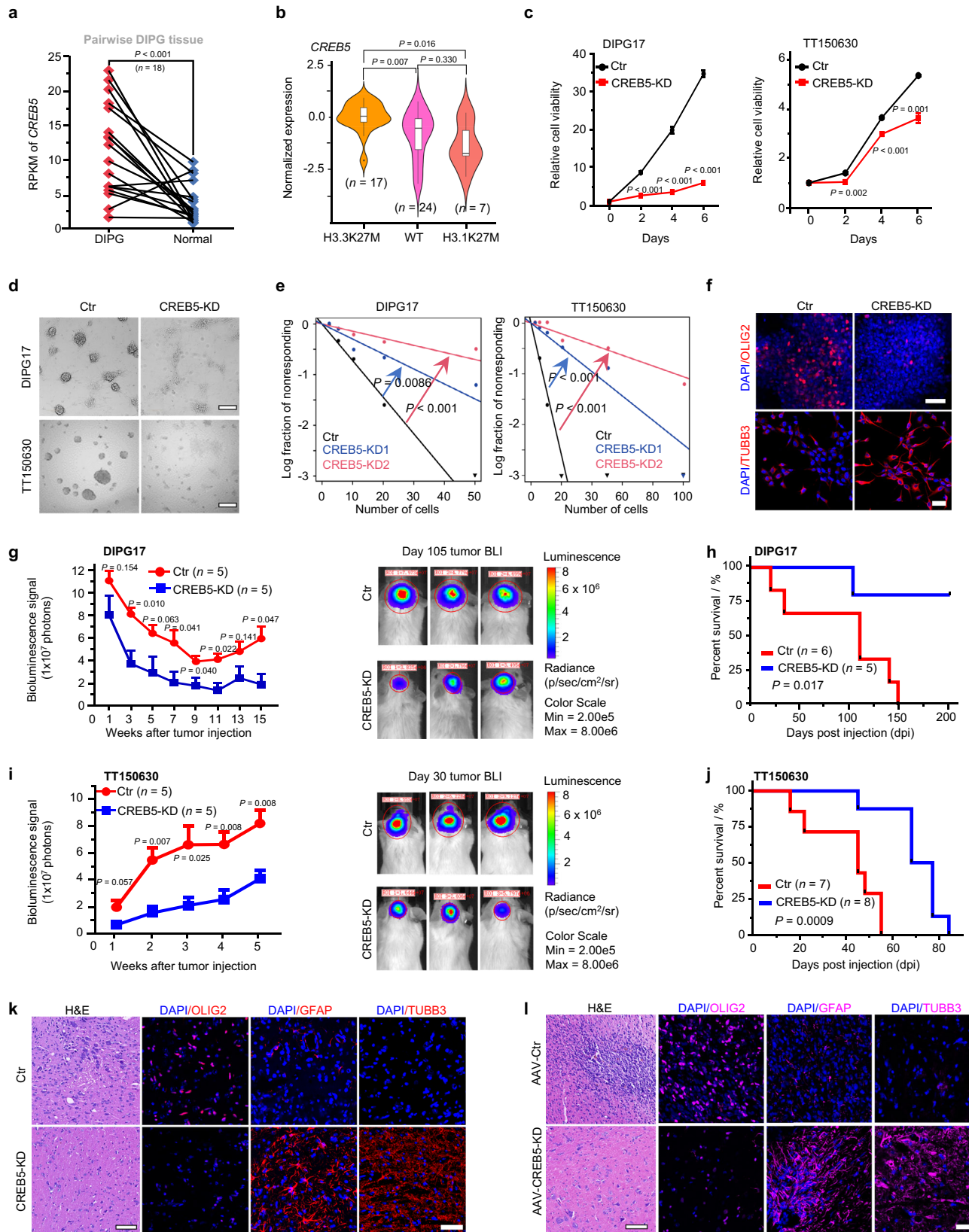
cytometry analysis based on annexin V-FITC/PI staining showed that the proportion of apoptotic cells was significantly increased upon *CREB5* knockdown compared to scramble control DIPG17 cells (Supplementary Fig. 3e). Finally, IF staining showed that *CREB5* KD inhibits the stemness of DIPG cells indicated by significantly reduced *OLIG2* expression, while inducing differentiation, indicated by increased expression of *TUBB3* (Fig. 2f). GO and GSEA analyses identified enrichment of AC and OC differentiation pathways in the *CREB5*-KD groups (Supplementary Fig. 3f, g), further supporting the role of *CREB5* in maintaining DIPG stemness through the regulation of stemness-related gene expression. Thus, disrupting *CREB5* function reduces both cell proliferation and stemness while promoting apoptosis and differentiation.

To examine whether *CREB5* knockdown affects the malignancy of H3.3K27M DIPG in vivo, we stereotactically implanted DIPG cells (stable *CREB5*-KD or scramble control DIPG17 or TT150630 cells) into the pons of immunocompromised mice. Moreover, in assessing the therapeutic potential of *CREB5*, we injected adeno-associated virus (AAV) containing shRNAs targeting *CREB5* into the TT150630 xenograft mice. In these xenograft mouse models, tumors with *CREB5* KD showed significantly decreased tumor sizes and prolonged survival time compared to the control group (Fig. 2g-j and Supplementary Fig. 3h, i). H&E and IF staining supported that tumors with *CREB5* KD compared to scramble control exhibited a significant decrease in the number of tumor cell nuclei and in the expression of human nuclei antigen (HNA) and proliferation marker *Ki67* in vivo (Fig. 2k, l and Supplementary Fig. 3j, k). Notably, IF staining showed that knockdown of *CREB5* resulted in a significantly decreased *OLIG2* level, accompanied by significantly increased *GFAP* and *TUBB3* levels in TT150630 and DIPG17 xenografts (Fig. 2k, l and Supplementary Fig. 3l), suggesting that *CREB5* KD reduces cancer stemness and promotes differentiation of H3.3K27M DIPG tumors.

Together, our findings demonstrated that *CREB5* functions as an upstream regulator of the oncogenic factor *ID1*, maintaining a malignant OPC/stem-like cell state and promoting tumor growth in H3.3K27M DIPG.

### *Creb5* is specifically expressed in normal forebrain neural progenitors

Previous reports of clinical observations have noted a restricted developmental window and specific pons location as informative features of DIPG, and these features have been interpreted to suggest a developmentally early etiology based on anatomically specific cell(s) of origin<sup>61-63</sup>. To investigate whether the expression pattern of oncogenic factor *CREB5* during murine gliogenesis is correlated with its high expression and stemness maintenance in DIPG, we next examined the spatiotemporal expression pattern of *Creb5* in the developing normal mouse brains.



Phylogenetic analysis showed that CREB5 protein sequences are highly conserved in mammals from the mouse to the human (Supplementary Fig. 4a). An analysis of prenatal mouse brain developmental mRNA expression data from ENCODE<sup>64</sup> showed that *Creb5* is specifically expressed in the mouse forebrain (*i.e.*, not in the hindbrain) during embryo development from E10.5 to E16.5 (*i.e.*, when gliogenesis

occurs in normal development)<sup>65–67</sup> (Fig. 3a). Additionally, ENCODE ChIP-seq data showed no H3K27me3 signals but significantly higher H3K27ac signals in the *Creb5* promoter region in the forebrain compared to the hindbrain and midbrain<sup>64</sup> (Fig. 3a). These transcriptomic and epigenetic findings both support that *Creb5* expression is restricted to the forebrain but not in the hindbrain during murine gliogenesis.

**Fig. 2 | CREB5 maintains an OPC/stem-like state and promotes tumor growth of H3.3K27M DIPG.** **a** Scatter plot showing the *CREB5* RPKM abundance of pairwise DIPG patients ( $n = 18$ ). The DIPG tumor tissues and paired normal tissues are from the same patient. **b** Normalized RNA expression of *CREB5* from UCSC Xena DIPG cohorts in H3.3K27M, H3.1K27M, and H3 WT DIPG clinical patients. For the box plots, the hinges denote the first and third quartiles, the whiskers correspond to minimum and maximum values (excluding outliers), and the horizontal line marks the median. **c** Viability of indicated cells ( $n = 3$  independent experiments). **d** Neural sphere formation of the Ctr or *CREB5* KD DIPG17 and TT150630 cells.  $N = 3$  independent experiments. Scale bars: 100  $\mu\text{m}$ . **e** Extreme limiting dilution assay in DIPG17 cells and TT150630 cells with or without *CREB5* KD. **f** Immunofluorescence images of OLIG2 and TUBB3 staining in DIPG17 cells with or without *CREB5* KD.

Scale bars: 50  $\mu\text{m}$ . **g–j** The bioluminescence activity in the DIPG17 (**g**) and TT150630 (**i**) PDX mouse models were plotted between *CREB5* KD and Ctr ( $n = 5$  mice in each group). Kaplan-Meier survival analysis from animals implanted with DIPG17 cells (**h**) and TT150630 cells (**j**) with or without *CREB5* KD in the pons. **k, l** H&E-stained or immunofluorescence images of pons sections from animals implanted with TT150630 cells (**k**) with or without *CREB5* KD and AAV-mediated shRNAs targeting *CREB5* or scramble control (**l**), examining anti-OLIG2, anti-GFAP, and anti- $\beta$ -tubulin. Scale bars: 50  $\mu\text{m}$ . Data presented as mean  $\pm$  s.e.m. of three independent experiments (**c**) or mean  $\pm$  s.e.m (**b, g, and i**); statistical significance was determined by a two-tailed paired Student's *t*-test (**a**), ordinary one-way ANOVA with Tukey test (**b**), two-tailed unpaired Student's *t*-test (**c, g, and i**), two-tailed likelihood-ratio test (**e**) or log-rank test (**h and j**). Source data are provided as a Source Data file.

At higher spatial resolution, an analysis of public data including simultaneous profiling of spatially resolved scRNA-seq and scATAC-seq data for the developing mouse brain<sup>68</sup> showed that *Creb5* is specifically expressed within the dorsal forebrain ventricular zone (VZ), a brain region/structure known to contain many progenitor cells such as neural progenitor cell (NPC) and OPC cells in the prenatal mouse brain<sup>65,69,70</sup> (Fig. 3b). We also noted a VZ-specific expression pattern for the OPC marker *Olig2* (Supplementary Fig. 4b). We then performed IF staining against *CREB5* and *OLIG2* in brain sections from various developmental stages (E11.5–E18.5) and found that *CREB5* is significantly enriched in the forebrain VZ but not in the hindbrain (Fig. 3c and Supplementary Fig. 4c, d). Analysis of scRNA-seq data from different developmental stages of prenatal mouse brain (E7.0–E18.0)<sup>70</sup> showed that a significant enrichment of *Creb5* in late radial glia cells (one kind of NPC cells) within the dorsal forebrain VZ (Fig. 3d). Collectively, *Creb5* is specifically expressed in forebrain neural progenitor cells in developing mouse brain.

### The presence of H3.3K27M induces *Creb5* expression in the hindbrain neural progenitors

*Creb5* is one of the syntenic genes from the highly conserved syntenic blocks (5.4 Mb) at the vertebrate *Hoxa* cluster<sup>71,72</sup>. In the mouse genome, *Creb5* is positioned in close proximity (1026 kb) to the *Hoxa* cluster on chromosome 6 (Supplementary Fig. 4e), a region known to be a target of PRC2-mediated gene silencing via the deposition of H3K27me3<sup>14,73–76</sup>. Notably, while H3K27me3 enrichment is present, PRC2 recruitment is absent at the promoter region of *Creb5* (Supplementary Fig. 4e–g), suggesting that the *Creb5* locus serves as a spreading site, rather than a nucleation site, for H3K27me3<sup>13,77–82</sup>.

To further investigate the correlation between *Creb5* expression and H3K27me3 modification, we performed a *Hoxa* cluster circular chromosome conformation capture (4C-seq) assay on NPCs derived from the hindbrain and forebrain of E13.5 mouse embryos. Our results reveal significant interactions (FDR < 0.05) between the *Hoxa* cluster and an upstream element of *Creb5* (-77 kb from the transcription start site) specifically in hindbrain NPCs (Supplementary Fig. 4h, i). This interaction is correlated with increased H3K27me3 enrichment and reduced *Creb5* expression in hindbrain NPCs, compared to forebrain NPCs (Supplementary Fig. 4j).

Collectively, these findings suggest that the silencing of *Creb5* in hindbrain progenitors may be mediated by long-range H3K27me3 spreading from the *Hoxa* cluster through three-dimensional (3D) genome organization.

Studies demonstrated that the main effect of oncohistone H3K27M is on the impaired spreading of H3K27me2/3 repressive marks<sup>8,11–14</sup>. Next, we investigated whether introducing the oncohistone H3.3K27M could trigger *Creb5* expression in developing mouse hindbrain neural progenitor cells by impairing the spreading of H3K27me3 from the *Hoxa* cluster. We analyzed the available H3K27me3 ChIP-seq and RNA-seq data from prior studies<sup>62</sup> of neural stem cells (NSCs) isolated from hindbrain or forebrain in E15.5 embryos

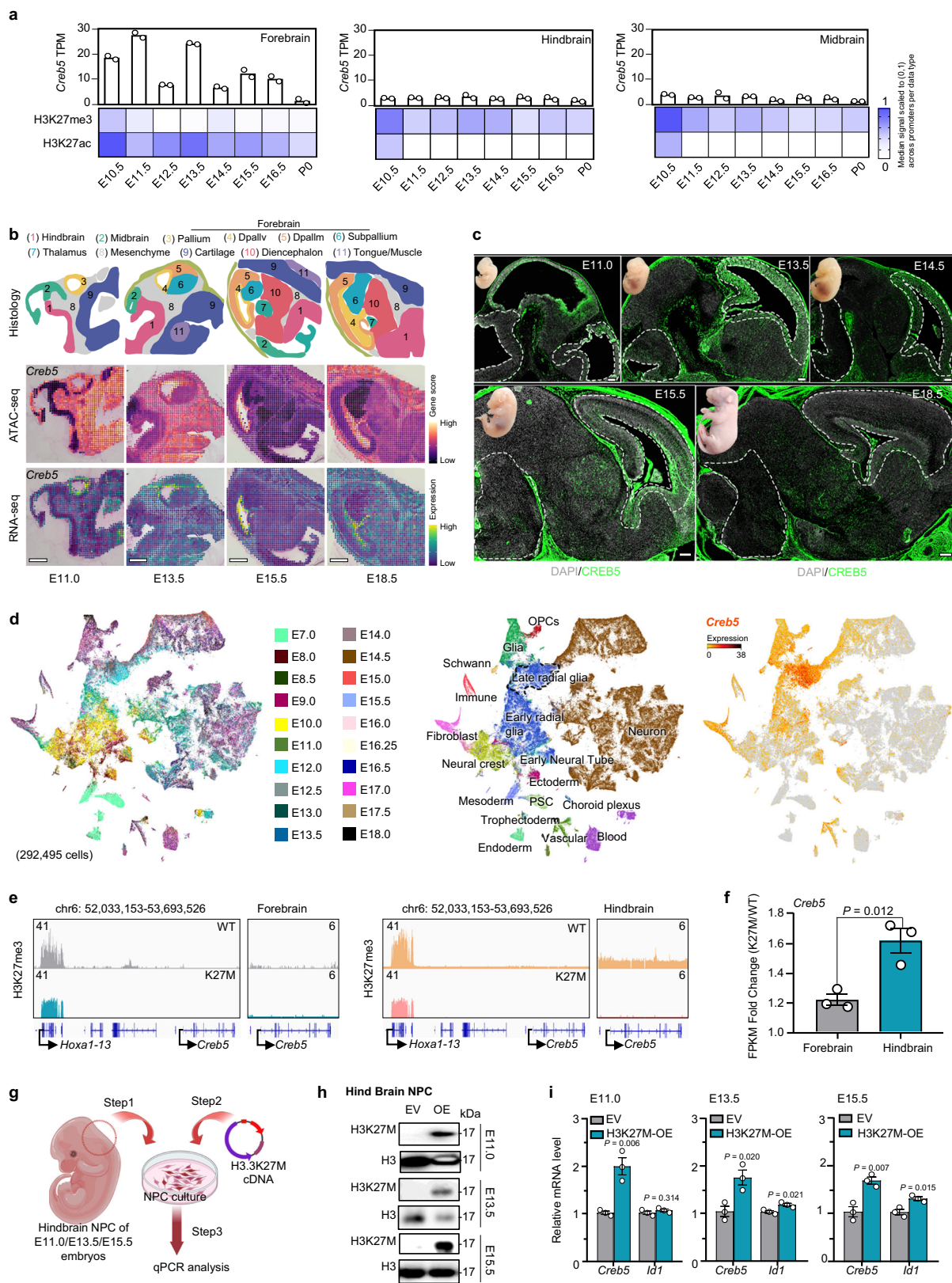
resulting from the mating of *H3f3a<sup>LSL-K27M-Tag/+</sup>* mice with *Nestin-Cre* mice (Supplementary Fig. 4d). The H3K27me3 ChIP-seq analysis revealed a significant reduction in H3K27me3 levels at the *Creb5* locus in hindbrain NSCs carrying the H3.3K27M mutation compared to those in the forebrain at E15.5 (Fig. 3e). And the nearby *Hoxa* cluster displayed a significantly reduced H3K27me3 levels in NSCs with the H3.3K27M mutation (Fig. 3e). Additionally, the RNA-seq data showed a significant increase of *Creb5* expression in hindbrain progenitors (1.6-fold) compared to minimal impact on *Creb5* expression in the forebrain progenitors (1.2-fold) upon the introduction of H3.3K27M (Fig. 3f). These results support that presence of oncohistone H3.3K27M impairs the H3K27me3 spreading from *Hoxa* cluster, consequently affecting the expression of the neighboring gene *Creb5* in hindbrain progenitors.

Then, we performed experiments by introducing H3.3K27M oncohistone expression into hindbrain progenitor cells of mouse embryos at E11.0, E13.5, and E15.5 stages (Fig. 3g, h and Supplementary Fig. 4d). This was done to explore whether the presence of H3.3K27M could induce *Creb5* expression in the mouse hindbrain. The expression of *Creb5* was significantly upregulated in the hindbrain with the presence of H3.3K27M across all three conditions, while its downstream target *Id1* expression was only increased at the E13.5 and E15.5 stages (Fig. 3i). This further suggested a potential role for H3.3K27M in inducing *Creb5* expression within the mouse hindbrain, raising the possibility that H3.3K27M similarly upregulates *CREB5* expression in human DIPG.

### Oncohistone H3.3K27M primes *CREB5* activation in DIPG

Next, we investigated whether H3.3K27M induces *CREB5* expression in DIPG. We first profiled the epigenetic landscape near the *CREB5* locus by aligning Hi-C (High-throughput Chromosome Conformation Capture) analysis of chromosome 7 (GSE162976)<sup>24</sup> with RNA-seq and ChIP-seq data of H3K27ac, H3K27me3, H3K4me1, H3K4me3, CTCF, and EZH2 derived from the same cell lines<sup>4,17,24,83</sup>. This approach allowed us to generate a comprehensive 3D genomic map around the *CREB5* locus in both DIPG patient-derived cell lines (DIPG XIII) and normal human astrocytes (NHAs) (Fig. 4a and Supplementary Fig. 5a). It's worth noting that there is no EZH2 binding at the H3K27me3-enriched region at the *CREB5* promoter in NHAs, suggesting that the H3K27me3 mark at the *CREB5* locus likely extended from the nearby *Hoxa* cluster (Fig. 4a).

*CREB5* is highly expressed in DIPG XIII and DIPG007, but not in NHAs from the RNA-seq track (Fig. 4a and Supplementary Fig. 5a). We observed a significant increase in the interaction between the promoter and the super-enhancer (SE) region of *CREB5* in DIPG XIII and DIPG007, which explains the elevated expression of *CREB5* in DIPG XIII and DIPG007 (Fig. 4a and Supplementary Fig. 5a). To be noted, this SE locates at *CREB5* intergenic region (chr7:28708923–28897199) with 188 kb length, which is highly enriched with H3K27ac and H3K4me1 (Fig. 4a). Indeed, a super-enhancer analysis revealed *CREB5*'s association with a SE in multiple H3.3K27M DIPG cells (Supplementary Fig. 5b). Consistent with this, the repressive mark H3K27me3 was absent at the *CREB5* locus in DIPG cells compared to in NHAs (Fig. 4a and



Supplementary Fig. 5a). These findings suggested that H3.3K27M may induce *CREB5* expression by altering epigenetic landscape, such as H3K27me3 spreading, at the *CREB5* locus.

To investigate whether H3.3K27M or H3.1K27M can induce *CREB5* expression, we introduced H3.3K27M, H3.3WT, H3.1K27M, and H3.1WT expression in PPCs. Notably, the introduction of H3.3K27M, not of

H3.1K27M or WT H3.3, H3.1, led to increased expression of *CREB5* in PPC cells as indicated by qPCR or immunoblotting assays (Fig. 4b, c and Supplementary Fig. 5c, d). Consistently, a previous work<sup>63</sup> utilizing human hindbrain neural stem cells to study the effects of H3.3K27M also showed that H3.3K27M induced *CRBE5* expression (Supplementary Fig. 5e).

**Fig. 3 | *Creb5* is specifically expressed in normal forebrain neural progenitors, but the presence of H3.3K27M induces *Creb5* expression in the hindbrain neural progenitors.** **a** RNA-seq and ChIP-seq profiles of different prenatal stages of mouse forebrain (left), hindbrain (middle), and midbrain (right) showing the mRNA expression (TPM) of *Creb5* and the H3K27me3 and H3K27ac signals at the promoter of *Creb5*. **b** Anatomic annotation (top) of major tissue regions based on the H&E images, UMAP embedding and spatial mapping of *Creb5* gene score (middle), and *Creb5* gene expression (bottom) at different developmental stages of mouse brain. The scRNA-seq and scATAC-seq data of developing mouse brain were analyzed from spatially resolved joint profiling of chromatin accessibility and gene expression<sup>58</sup>. Scale bars: 1000  $\mu$ m. Dpally, ventricular zone of dorsal pallium. DPallm, mantle zone of dorsal pallium. **c** Immunofluorescence of sagittal developing murine brain sections showing CREB5 dynamic expression in embryonic forebrain and hindbrain. Image shown is representative of  $n = 3$  independent replicates of experiments with similar results. Scale bars: 100  $\mu$ m. **d** UMAP visualization of different mouse brain development stage (left), different cell clusters (middle), and *Creb5* expression

(right) (<http://www.mousebrain.org/development/>). **e** IGV screenshot of the locus from *Hoxa* cluster to *Creb5* showing the signal tracks of H3K27me3 with or without H3.3K27M expression in forebrain and hindbrain mNSC neurospheres from previous study<sup>62</sup>. **f** FPKM fold change (H3K27M/WT) of *Creb5* with or without H3.3K27M overexpression in forebrain and hindbrain mNSC neurospheres from previous study<sup>62</sup>. **g** Schematic for the introduction of H3.3K27M oncohistone in the hindbrain NPC cultures. **h** Immunoblotting analysis of indicated proteins in the hindbrain mNPC cultures with or without H3.3K27M introduction. Experiments were repeated three times independently with similar results. **i** qPCR analysis of *Creb5* and *Id1* with or without H3.3K27M OE in the hindbrain mNPC cells. Data presented as mean  $\pm$  s.e.m. of three independent experiments, statistical significance was determined by a two-tailed unpaired Student's *t*-test (**f** and **i**). Experiments were repeated three times independently with similar results (**h**). Panel **g** created in BioRender. Zhou, W. (2025) <https://BioRender.com/a99h972>. Source data are provided as a Source Data file.

We then performed H3K27M, H3K27me3, and H3K27ac CUT&Tag assays in PPCs with or without the introduction of H3.3K27M to investigate how H3.3K27M alters the epigenetic landscape (Supplementary Fig. 5f). A genome-wide correlation analysis suggested that epigenetic profiles of H3.3K27M, H3K27me3, and H3K27ac observed in H3.3K27M-expressing PPC cells clustered closely to those seen in primary DIPG (Supplementary Fig. 5g), consistent with previous studies indicating genome-wide epigenetic reprogramming in DIPGs by oncohistone<sup>19,63</sup>. Next, we examined whether H3.3K27M is present at the *CREB5* locus and its impact on H3K27me3 spreading. The CUT&Tag analysis revealed that H3.3K27M was enriched at the promoter and intergenic regions of *CREB5* whereas minimal to no H3K27me3 was detected around the *CREB5* locus ( $\text{Log}_2$  Fold Change = -2.6, FDR = 0.027) in PPC cells overexpressing H3.3K27M compared to control PPC cells (Fig. 4d and Supplementary Fig. 5h). These data supported that oncohistone H3.3K27M impedes H3K27me3 spreading surrounding *CREB5* locus, consequently induces *CREB5* expression.

Furthermore, we established the H3.3K27M KD DIPG17 cells and H3.1K27M KD DIPG-IV cells respectively to investigate whether disrupting H3.3K27M or H3.1K27M can impair *CREB5* expression in DIPG cells. qPCR and western blot assays showed that H3.3K27M KD resulted in significantly decreased *CREB5* expression in DIPG17 cells compared to scramble control (Fig. 4e, f). However, H3.1K27M KD does not affect *CREB5* expression in DIPG-IV cells (H3.1K27M subtype) (Supplementary Fig. 5i). CUT&Tag and ChIP-seq analysis of H3K27me3 revealed a significant increase in H3K27me3 levels at the *CREB5* promoter ( $\text{Log}_2$  Fold Change = 2.02, FDR = 0.02) following H3.3K27M KD/KO in DIPG17 and DIPG XIII cells<sup>33</sup> (Fig. 4g and Supplementary Fig. 5j-l). This further supported that the presence of oncohistone H3.3K27M, rather than H3.1K27M, at the *CREB5* locus, induces *CREB5* expression by preventing H3K27me3 spreading.

In summary, these findings demonstrated that oncohistone H3.3K27M is incorporated at the *CREB5* locus, reducing H3K27me3 signals, creating a permissive chromatin environment conducive to the transcriptional induction of *CREB5*.

### CREB5 regulates genes associated with decreased survival time in DIPG patients

CREB5 is a transcription factor known for its high affinity for cAMP-response elements (CREs)<sup>28–30</sup>. We performed CUT&Tag assays using antibodies against CREB5, H3K27ac, H3K27me3, H3K9me2, and ATAC-seq to explore CREB5 genome-wide distribution and its association with chromatin. The CUT&Tag analysis revealed that CREB5 was enriched at active promoter (3282 peaks) and enhancer (1349 peaks) regions of the genome, which largely colocalize at regions with open chromatin accessibility (ATAC-seq) and active histone modifications (H3K27ac and H3K4me3<sup>33</sup>) (Fig. 5a). We also conducted a CUT&RUN

assay to evaluate CREB5 chromatin binding, utilizing the same DIPG17 cell line employed in the CUT&Tag assay. A comparative genome-wide analysis of chromatin binding profiles from both assays demonstrated a strong correlation between the CUT&Tag and CUT&RUN data for CREB5 binding (Pearson's correlation coefficient,  $R = 0.99$ ; Supplementary Fig. 6a-c).

Interestingly, CREB5-binding enhancer regions showed noticeable H3K9me2 (aka facultative heterochromatin) signals, suggesting that CREB5 is capable of binding with less accessible chromatin regions (Fig. 5a and Supplementary Fig. 6d, e). Consistently, IF results showed the co-localization of CREB5 and H3K9me2 in DIPG cells (Supplementary Fig. 6f). Moreover, CREB5 was found to co-localize with H3K9me2 in both intergenic and intronic regions, during both the primed state—characterized by weak ATAC-seq signals and the absence of H3K27ac—and the active state, marked by strong ATAC-seq and H3K27ac signals of facultative heterochromatin<sup>34</sup> (Supplementary Fig. 6g, h). Our analysis indicates that genome-wide facultative heterochromatin exhibits a limited association with CREB5 in DIPG cells (Supplementary Fig. 6e), suggesting that CREB5 likely serves distinct functional roles within facultative heterochromatin compared to promoter regions.

Further analysis of our CREB5 CUT&Tag and RNA-seq datasets for CREB5 KD and control conditions revealed 451 upregulated genes and 469 downregulated genes in CREB5 KD DIPG cells compared to scramble control cells, all of which exhibited significant CREB5 binding signals within their respective promoter regions (Fig. 5b). GO annotations of these downregulated genes upon CREB5 KD suggested their involvement in the regulation of transcription, cell cycle, and neural progenitor proliferation (Fig. 5b). Notably, these genes include those associated with stemness such as *ID1*, *ID3*, *ETV1*, *EGR1*, and *KLF4*, as well as malignant oncogenes like *JUN*, *FOS/FOSB*, *EGFR*, and *NFIC* (Fig. 5b). Moreover, CREB5 binds at *ID1* promoter and colocalizes with active histone marks (Fig. 5c).

We subsequently explored potential associations of CREB5-regulated genes with patient survival by performing a subgroup analysis. Tumor samples from the UCSC Xena cohort<sup>58</sup> were divided into “decreased survival” and “increased survival” subgroups based on the median value of survival time (Fig. 5d). Further we examined the expression patterns of CREB5 direct-regulated genes within these subgroups. We found that genes downregulated by CREB5 KD were significantly enriched in the “decreased survival” subgroup, while those upregulated by CREB5 knockdown were significantly enriched in the “increased survival” subgroup (Fig. 5e, f and Supplementary Data 2). Taken together, these findings support that the elevated *CREB5* levels resulting from oncohistone H3.3K27M drive target binding (such as *ID1*) and oncogenic transcriptional changes, ultimately contributing poor clinical outcomes in H3.3K27M DIPGs.

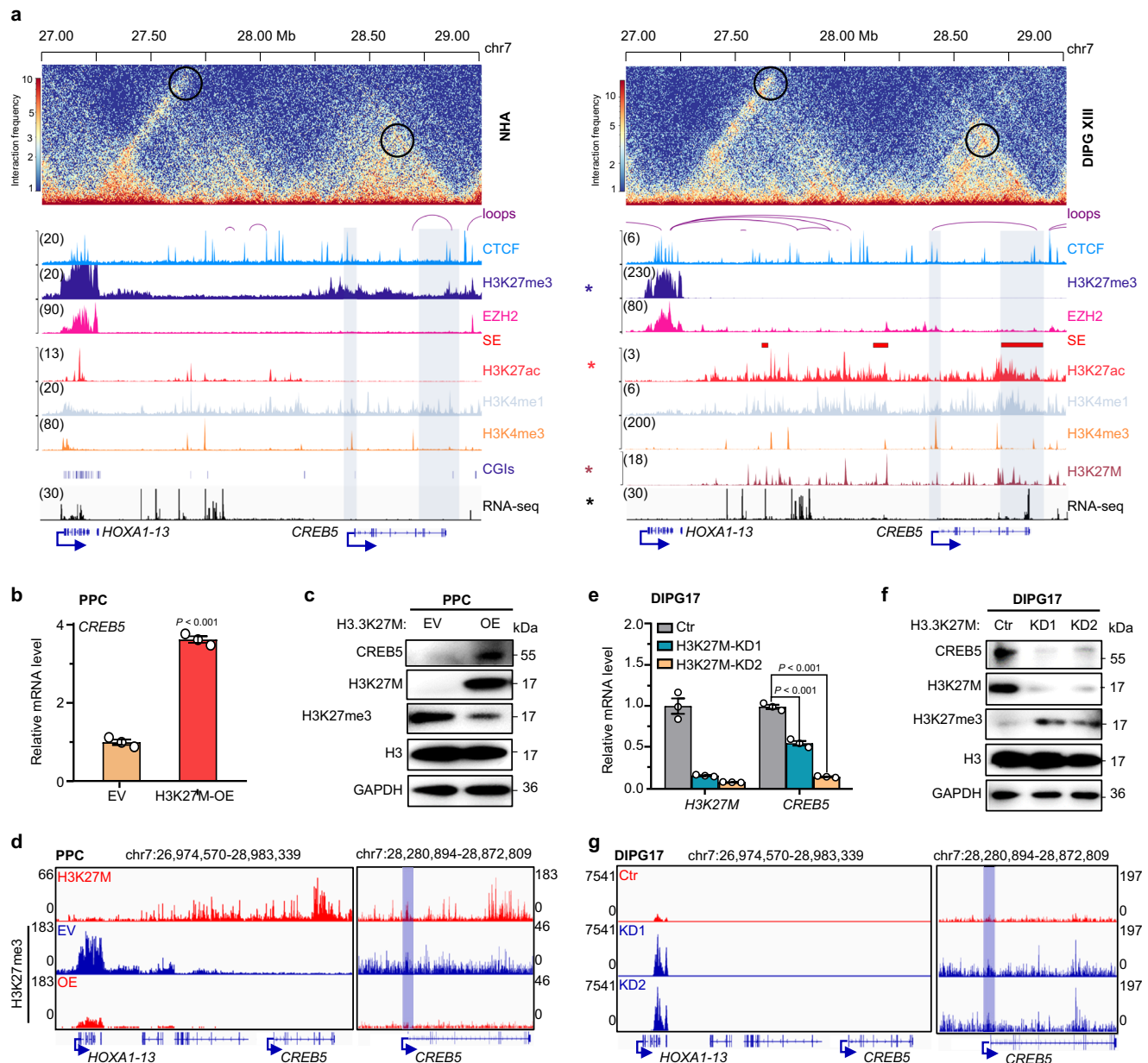


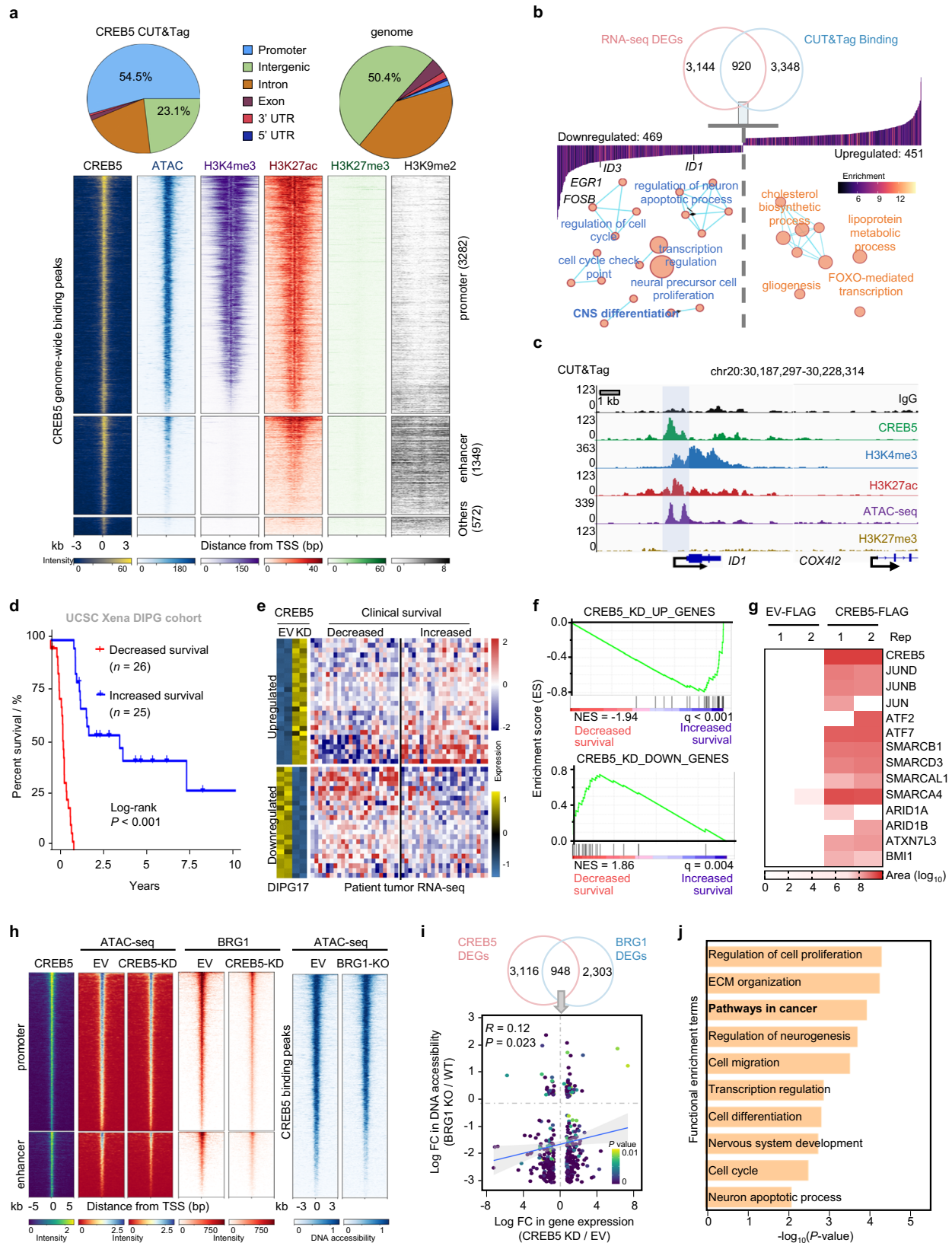
**Fig. 4 | Oncohistone H3.3K27M primes *CREB5* activation in DIPG.** **a** Hi-C contact maps, RNA-seq, and ChIP-seq tracks of CTCF, H3K27me3, EZH2, H3K27ac, H3K4me1, H3K4me3, CpG islands (CGIs), and super-enhancer (SE) at *HOXA1-13* and *CREB5*. The shading on the left denotes the promoter region of *CREB5*, while the shading on the right indicates the super-enhancer associated with *CREB5*. **b** qPCR analysis of *CREB5* with or without H3.3K27M overexpression in PPC cells. **c** Immunoblotting analysis of the indicated proteins with or without H3.3K27M overexpression in PPC cells. **d** IGV tracks displaying H3K27M and H3K27me3 profiles in PPC cells at *CREB5* locus and its neighboring *HOXA1-13* gene cluster, with or without H3.3K27M OE. The blue shading denotes the differential binding peak of

H3K27me3 at the promoter of *CREB5*. **e** qPCR analysis of *H3.3K27M* and *CREB5* with or without H3.3K27M KD in DIPG17 cells. **f** Immunoblotting analysis of the indicated proteins with or without H3.3K27M KD in DIPG17 cells. **g** IGV tracks displaying H3K27me3 profile in DIPG17 cells at *CREB5* and its neighboring *HOXA1-13* gene cluster, with or without H3.3K27M KD. The blue shading denotes the differential binding peak of H3K27me3 at the promoter of *CREB5*. Data presented as mean  $\pm$  s.e.m. of three independent experiments, statistical significance was determined by a two-tailed unpaired Student's *t*-test (**b** and **e**). Experiments were repeated three times independently with similar results (**c** and **f**). Source data are provided as a Source Data file.

### CREB5 associates with SWI/SNF complex to regulate oncogenic transcriptional changes in H3.3K27M DIPG

CREB5 often formed heterodimers with other transcription factors with bZIP domain<sup>28</sup>. To gain insights into whether CREB5 associates with other co-partners to drive the oncogenic transcriptional changes, we next analyzed DNA motifs in 5,205 CREB5 peaks. CREB5 binding motif showed a remarkable similarity to those of the bZIP family (AP-1 and ATF family) members and E2F which are well-known oncogenes or regulators of the cell cycle in tumorigenesis<sup>85,86</sup>, suggesting their co-binding (Supplementary Fig. 6i).

We then performed an immunoprecipitation-mass spectrometry (IP-MS) assay in DIPG17 cells to identify potential binding partners of CREB5. The IP-MS analysis revealed a total of 358 candidate interacting partners, with functional analysis indicating their involvement in transcription regulation, including chromatin remodeling, and pathways related to cancer (Supplementary Fig. 6j). In alignment with prior research<sup>28,30,36</sup>, we found that CREB5 interacts with members of the AP-1 family (JUN, JUND, and JUNB) and ATF family (ATF2 and ATF7) (Fig. 5g and Supplementary Data 3). Interestingly, multiple subunits of the SWI/SNF complex were among the candidate CREB5-interacting



proteins (SMARCA4, SMARCD3, SMARCAL1, SMARCB1, ARID1A, and ARID1B) (Fig. 5g and Supplementary Data 3).

Previous studies showed that SWI/SNF is the vulnerable target for DIPG/DMG treatment<sup>27,87</sup>. BRG1 serves as the catalytic ATPase subunit within the SWI/SNF complex<sup>88</sup>. In order to investigate whether CREB5 colocalizes with BRG1 to regulate oncogenic transcriptional changes in

H3.3K27M DIPG, we first analyzed CREB5 and BRG1 CUT&Tag data. The analysis revealed co-localization of CREB5 and BRG1 in the regions where CREB5 binds, and 78% (4076/5203) of CREB5 binding peaks have BRG1 binding (Fig. 5h and Supplementary Fig. 6k). Intriguingly, 82% (753/920) of CREB5 direct-regulated genes have BRG1 binding (Supplementary Fig. 6k), including stemness-associated genes (*ID1/3*, *ETV1*,

**Fig. 5 | CREB5 associates with the chromatin remodeling complex SWI/SNF, leading to oncogenic transcriptional changes in H3.3K27M DIPG.** **a** CUT&Tag profiles from DIPG17 cells showing the CREB5 binding peaks for CREB5, ATAC-seq, H3K4me3, H3K27ac, H3K27me3, and H3K9me2. Pie charts showing the percentage of CREB5 binding at the genome. **b** The Venn diagram (top) showing the CREB5 directly regulated genes. Waterfall plot (middle) of 920 genes that exhibited significant CREB5 binding signals within their respective promoter regions, which were also significantly regulated by CREB5. GO analysis of these genes was performed (bottom). **c** IGV tracks for CREB5, H3K4me3, H3K27ac, H3K27me3 CUT&Tag, and ATAC-seq in DIPG17 cells at *ID1* and its neighboring gene *COX4L2* gene loci (negative control, in black). **d** Kaplan-Meier survival curves for DIPG patients in the UCSC Xena patient cohort separated into decreased and increased survival groups. **e** Heatmaps illustrating CREB5-regulated genes in control (Ctr) or CREB5 KD DIPG17 cells (left panel), alongside clinical DIPG patient RNA-seq dataset depicting subgroups of decreased survival or increased survival (right panel). **f** GSEA analysis showing enrichment of CREB5\_KD\_upregulated genes in the “increased survival”

group (top) and CREB5\_KD\_downregulated genes in the “decreased survival” group (bottom). **g** Heatmap showing the spectral area with  $\log_{10}$  normalization of CREB5 interactome.  $N = 2$  independent experiments. **h** Heatmap representation of CREB5 CUT&Tag signal, ATAC-seq signal and BRG1 CUT&RUN signal with or without CREB5 KD at CREB5 peaks regions sorted by promoter and enhancer region. The right panel showing ATAC-seq signals at CREB5 peaks with or without BRG1 KO. **i** Correlation plot illustrating the relationship between the differential DNA accessibility at selected genes’ promoter regions following BRG1 KO and the corresponding changes in gene expression upon CREB5 KD. The selected genes represent the overlap between differentially expressed genes (DEGs) identified in CREB5 KD and BRG1 KO, as illustrated in the upper Venn diagrams. The  $p$  value and correlation coefficient were calculated using Pearson’s correlation. The error bands indicate 95% CIs as shades based on standard error. **j** Gene Ontology (GO) and KEGG analysis on genes from (i) using DAVID. The statistical significance was determined by a two-tailed unpaired Student’s  $t$ -test (i) or two-tailed hypergeometric test (j).

*EGR1*, *NES*, and *KLF4*) and oncogenes (*JUN/JUNB*, *FOS/FOSB*, *EGFR*, and *NFIC*), indicating the colocalization of CREB5 and the SWI/SNF complex on chromatin.

Both ATAC-seq and BRG1 CUT&Tag analyses showed that CREB5 knockdown in DIPG17 cells resulted in a significant reduction in DNA accessibility, evidenced by the loss of 3129 peaks and the gain of 310 peaks, as determined using the DESeq2 statistical method in DiffBind ( $p$  value  $< 0.05$ ) and in the extent of BRG1 chromatin binding at genes (e.g., *CREB5*, *NKX2-2*, *ETVI*, *EGR1*, and *ID1*) co-occupied by CREB5 and BRG1 (Fig. 5h and Supplementary Fig. 6l-o). Additionally, the chromatin accessibility of these co-binding genomic loci was significantly reduced upon BRG1 KO<sup>87</sup> (Fig. 5h). Moreover, in DIPG cells, for genes regulated by both CREB5 and BRG1, alterations in DNA accessibility mediated by BRG1 exhibit a positive correlation with transcriptional changes governed by CREB5 (Pearson’s correlation:  $R = 0.12$ ,  $P = 0.023$ ) (Fig. 5i). GO analysis revealed that these genes play roles in both transcriptional dysregulation in cancer and stemness (Fig. 5j). Thus, these results supported the association of CREB5 with the SWI/SNF complex in the regulation of oncogenic transcription in H3.3K27M DIPG.

### ABBV-075 inhibits CREB5 expression by disrupting its super-enhancer activity

Considering that CREB5 KD inhibits tumor growth in H3.3K27M DIPG xenograft models, targeting CREB5 presents a promising therapeutic approach. Our Connectivity Map analysis (L1000) pinpointed BRD4 inhibitor, JQ1, to have similar effects on the transcriptome of DIPG cells as CREB5 depletion<sup>79</sup>. To explore this, we first examined the presence of BRD2, BRD4, H3K27ac, and H3.3K27M enrichment at the *CREB5* super-enhancer locus by analyzing publicly available DIPG datasets<sup>80</sup> (Fig. 6a). Our analyses also revealed that JQ1 exerted a significant inhibitory impact on *CREB5* expression in H3.3K27M DIPG compared with H3.1K27M DIPG, which shows low expression and no super-enhancers enriched in *CREB5* (Fig. 6a and Supplementary Fig. 7a). Consistently, we demonstrated that JQ1 treatment led to the downregulation of *CREB5* expression and stemness markers (Fig. 6b). However, JQ1’s limited half-life, high dosage requirements, and potential toxicity have hindered its clinical development<sup>81–83</sup>. Given *CREB5*’s association with super-enhancers in H3.3K27M DIPG and BRD4’s ability to target these regions via its twin bromodomains<sup>55,89</sup>, we initiated a drug screening to identify a BRD4 inhibitor specifically targeting *CREB5* and inhibiting DIPG cell growth (Fig. 6c).

We screened publicly available BRD4 inhibitors (BRD4i) from the MCE bioactive compound library to identify a potent candidate capable of suppressing *CREB5* expression in DIPG cells. The efficacy of each inhibitor was assessed by measuring *CREB5* mRNA levels via qPCR analysis. This screening process resulted in the identification of five potent BRD4i candidate compounds (Fig. 6d and Supplementary

Data 4). We then conducted cell viability assays on DIPG17 cells and PPC cells to evaluate the inhibitory potential and toxicities of these five drugs, along with two positive controls (compounds 12 and 16) (Fig. 6e). Among these five candidate compounds, compound 5 (ABBV-075, aka mivebresib<sup>90,91</sup>) had significant growth inhibition to DIPG cells with minimal toxicity to normal PPC cells (Fig. 6e and Supplementary Fig. 7b). Consistent with these findings, immunoblotting analysis revealed that treatment with ABBV-075 at the specified time points and concentrations resulted in a marked reduction of CREB5 and H3K27ac protein levels in DIPG17 cells (Fig. 6f, g).

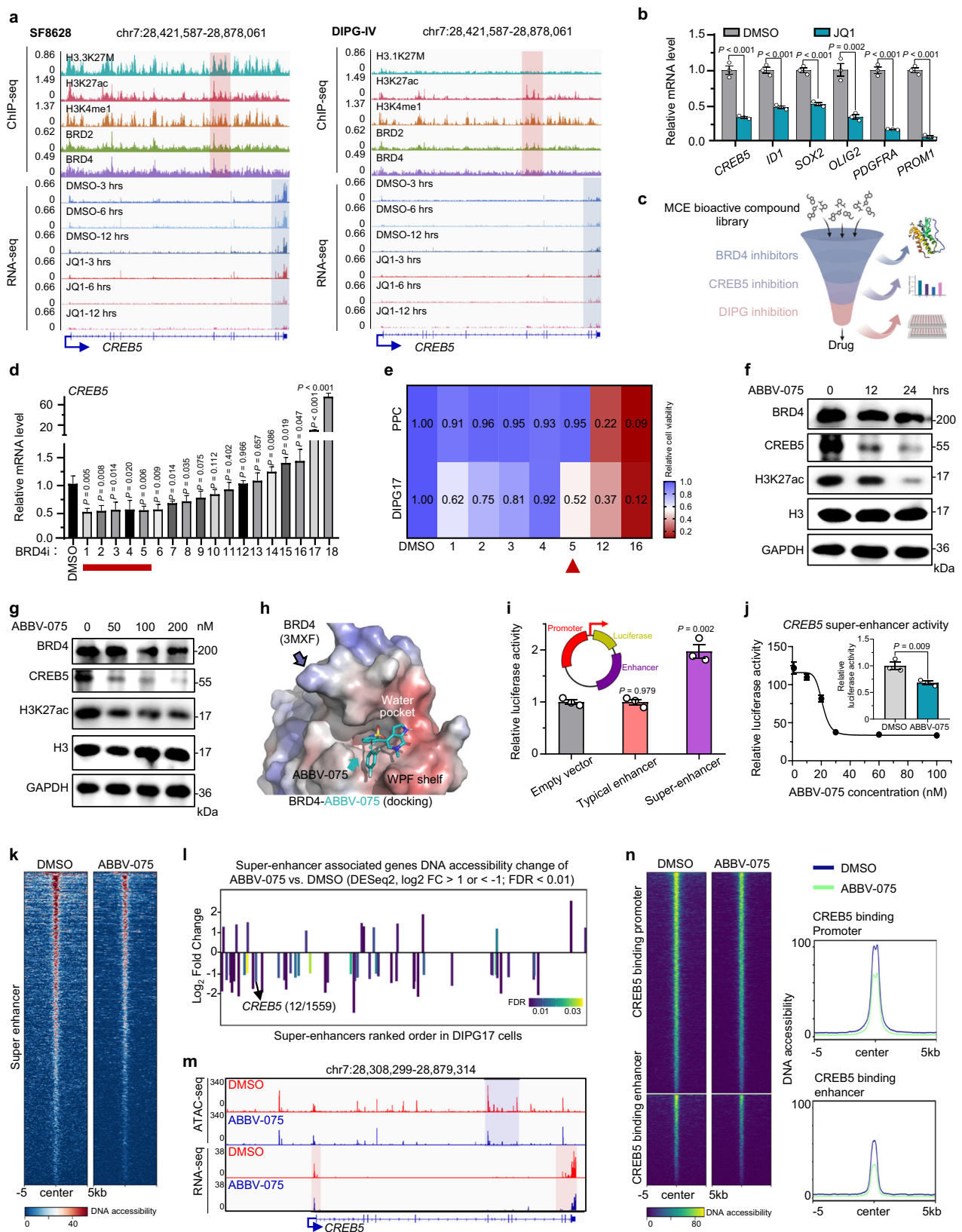
To reveal the inhibition mechanism of ABBV-075 on BRD4, we used the molecular docking assay to examine whether ABBV-075 exhibited a binding pattern similar to JQ1 (Fig. 6h and Supplementary Fig. 7c). This predicts a potential interaction between ABBV-075 and the WPF shelf (amino acids recognizing H3K27ac) within the water pocket of BRD4 (Fig. 6h and Supplementary Fig. 7d).

To assess the inhibitory effects of ABBV-075 on *CREB5* super-enhancer, we also constructed a dual-luciferase reporter system using *CREB5* promoter (2 kb, chr7: 28448138-28450138) and enhancers including super-enhancer (2 kb, chr7:28725000-28727000) and typical enhancer (2 kb, chr7: 28771000-28773000) (Fig. 6i and Supplementary Fig. 7e). Our reporter assay results showed that its super-enhancer significantly enhanced the promoter activity of *CREB5* compared to its typical enhancer counterpart (Fig. 6i). Given the high dosage requirements of current BET inhibitors (e.g., more than 300 nM for JQ1), there is a need for more potent inhibitors to achieve effective super-enhancer inhibition<sup>92–94</sup>. Intriguingly, ABBV-075 achieved its maximal inhibitory effect on the *CREB5* super-enhancer at a concentration of 20 nM (Fig. 6j), highlighting the potent efficacy of ABBV-075 in inhibiting CREB5 super-enhancer activity via targeting BRD4.

### ABBV-075 reduces DNA accessibility at the CREB5 super-enhancer

We performed RNA-seq and ATAC-seq analyses on DIPG17 cells treated with or without ABBV-075 (Supplementary Fig. 7f). RNA-seq data revealed that ABBV-075 induces the expression of differentiation-associated genes (e.g., *TUBB3*, *SEMA3C*, *SYNI*) while reducing the expression of stemness-associated genes (e.g., *PROM1*, *OLIG2*, *PDGFRA*) (Supplementary Fig. 7g). GO and GSEA further demonstrated that ABBV-075 treatment downregulated stemness-related pathways and upregulated those associated with differentiation (Supplementary Fig. 7h, i).

ATAC-seq analysis indicated a global decrease in DNA accessibility at promoter and enhancer regions, including super-enhancers (Fig. 6k and Supplementary Fig. 8a). Differential peak analysis between treated and untreated cells showed a significant enrichment of altered H3K27ac-marked peaks in intergenic and intronic regions (Supplementary Fig. 8b,c). Notably, 87.17% of super-enhancer-associated



ATAC-seq peaks exhibited a significant reduction in accessibility following ABBV-075 treatment compared to the control group (Supplementary Fig. 8c, d). Collectively, these findings suggest that ABBV-075 restricts enhancer accessibility, consequently downregulating the expression of stemness-associated genes while upregulating genes involved in differentiation in DIPG cells.

To further investigate ABBV-075's impact, we ranked super-enhancer-associated genes with altered accessibility, excluding those with no change. This analysis identified *CREB5* as one of the top-ranked genes with significantly reduced accessibility (Log<sub>2</sub> Fold Change = -1.41, FDR = 0.0096; ranked 12th out of 1559) (Fig. 6l). Importantly, among the top 12 super-enhancer-associated genes, only *CREB5* was significantly

**Fig. 6 | Disrupting the super-enhancers using ABBV-075 inhibits *CREBS* expression, consequently preventing H3.3K27M DIPG tumor growth.**

**a** Representative IGV tracks for RNA-seq with vehicle or JQ1 treatment at a time-course and indicated ChIP-seq in DIPG cells at *CREBS* gene loci. **b** qPCR analysis of indicated genes with vehicle or JQ1 (300 nM) treatment for 24 hours in DIPG17 cells. **c** Schematic of BRD4 inhibitor screening strategy. **d** qPCR analysis of *CREBS* expression treated with series compounds for 24 hours in DIPG17 cells. **e** Heatmap showing the relative cell viability of DIPG17 cells and normal PPC cells treated with indicated compounds for 48 hours ( $n = 3$ ). **f, g** Immunoblotting analysis of the indicated proteins with ABBV-075 (100 nM) treatment at indicated time points (**f**) and with mentioned concentrations of ABBV-075 for 24 hours (**g**) in DIPG17 cells. **h** The overall structure of molecular docking ABBV-075 (shown in blue) in complex with BRD4 protein (PDB: 3MXF). **i** Bar graph depicting luciferase activity of indicated reporter constructs in 293T cells. **j** Line graph depicting the *CREBS* promoter luciferase activity with ABBV-075 treatment at various concentrations. The insert

bar graph shows the luciferase activity treated with 100 nM ABBV-075 for 24 hours. **k** ATAC-seq profiles from DIPG17 cells showing the DNA accessibility for super-enhancer regions with or without ABBV-075 treatment (100 nM) for 24 hours. **l** Bar plot showing the fold change of ATAC-seq peaks with or without ABBV-075 treatment at pre-ranked super-enhancer associated genes in DIPG17 cells.

**m** Representative IGV tracks for ATAC-seq and RNA-seq with vehicle or ABBV-075 treatment in DIPG17 cells at *CREBS* gene loci. **n** ATAC-seq profiles from DIPG17 cells showing the DNA accessibility for *CREBS* binding promoter and enhancer regions with or without ABBV-075 treatment. Metagene plot showing the average signal for ATAC-seq at *CREBS*-binding promoter and enhancer regions with or without ABBV-075 treatment. Data presented as mean  $\pm$  s.e.m. of three independent experiments (**b, d, i, and j**), statistical significance was determined by a two-tailed unpaired Student's *t*-test (**b, d, i, and j**). Experiments were repeated three times independently with similar results (**f and g**). Panel **c** created in BioRender. Zhou, W. (2025) <https://BioRender.com/q17x870>. Source data are provided as a Source Data file.

correlated with poor prognosis in DIPG (Supplementary Table 2). These findings suggest that ABBV-075 preferentially disrupts the DNA accessibility of super-enhancers, including the *CREBS* locus, in DIPG cells.

By correlating ATAC-seq-derived accessible chromatin regions with RNA-seq expression levels of their nearest associated genes, we identified 258 significant peak-gene associations and their corresponding target genes (Supplementary Fig. 8e). The correlation analysis showed a positive association between changes in DNA accessibility (ATAC-seq) and gene expression (RNA-seq) in DIPG17 cells treated with ABBV-075 (Supplementary Fig. 8f). Specifically, the reduced accessibility at the *CREBS* super-enhancer was strongly associated with decreased *CREBS* expression post-ABBV-075 treatment (Fig. 6m). Furthermore, ABBV-075 treatment led to the inhibition of DNA accessibility at *CREBS* binding sites within both promoter and enhancer regions (Fig. 6n). Thus, these findings suggest that impaired DNA accessibility at *CREBS* super-enhancer by ABBV-075 may contribute to the suppression of *CREBS* expression, thereby impeding the growth of H3.3K27M DIPG tumors.

**Combinatorial approach with ABBV-075 and BRG1 inhibition shows synergistic effects for H3.3K27M DIPG treatment**

Next, we assessed the effect of ABBV-075 on the proliferation of various DIPG cells and PPCs using cell viability and neurosphere assays with JQ1, a well-known BRD4 inhibitor<sup>92–94</sup> (Fig. 7a, b). ABBV-075 exhibited significantly lower toxicity towards PPC cells and displayed a significant reduced IC50 in DIPG when compared to JQ1 (Fig. 7a, b and Supplementary Table 3), suggesting ABBV-075 is a potential candidate for treating H3.3K27M DIPG. Moreover, the ABBV-075 treatment resulted in reduced OLIG2 and ID1 expression, as indicated by immunoblotting (Supplementary Fig. 9a), implying a decline in the stemness state following treatment in DIPG17. And DIPG17 cells treated with ABBV-075 exhibited a neurite-like process, a phenomenon indicative of glioma stem cell differentiation<sup>4</sup>, as observed under the bright-field microscope (Supplementary Fig. 9b). Further, we treated TT150630 xenograft mice with ABBV-075 (1 mg/kg, oral gavage) every 3 days for a total of 8 times (Supplementary Fig. 9c). ABBV-075 treatment significantly inhibited tumor growth indicated by a reduced bioluminescence compared to the vehicle group (Fig. 7c, d). ABBV-075 treatment significantly improved the survival compared to the vehicle control (Fig. 7e).

Pharmacologically targeting BRG1 has been shown to reduce DMG tumor growth in vivo, as evidenced by multiple studies<sup>27,87,95</sup>. Given the interaction between *CREBS* and BRG1 for oncogenic transcription regulation, we investigated whether combining ABBV-075 with the BRG1 inhibitor (BRM014) would demonstrate synergistic effects in inhibiting the proliferation of H3.3K27M DIPG cells. Utilizing the combinatorial index and Bliss independence model<sup>96,97</sup>, we evaluated the impact of combined ABBV-075 and BRM014 treatment on cell viability in DIPG17 and TT150714 cells. Remarkably, even at low doses

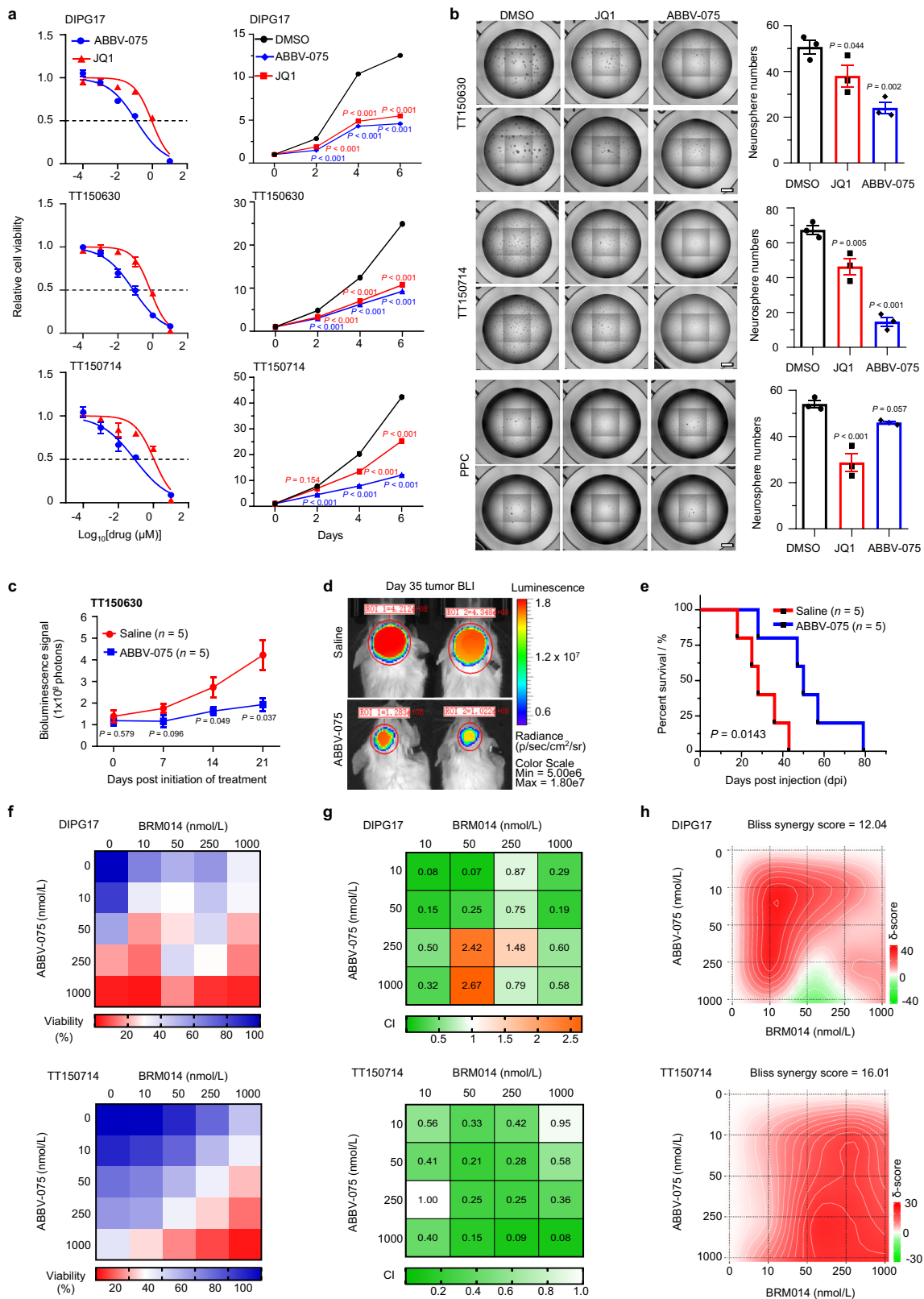
of both drugs, the combination therapy exhibited significant inhibitory effects on cell viability in both DIPG cells (Fig. 7f). This was further evaluated by calculating the combinatorial index (CI) using compusyn software (<https://www.combosyn.com>) for each pairwise combination, identifying likely synergistic areas within the combinatorial matrix, highlighted in green on the heat map (Fig. 7g). A summary synergy score was calculated as the average excess response due to drug interactions above expectations, indicating a significant level of formal synergy in DIPG17 (Bliss: 12.04) and TT150714 (Bliss: 16.01) DIPG cells (Fig. 7h).

Collectively, these findings suggested that ABBV-075 exerts its anti-tumor efficacy by potentially disrupting super-enhancer activity at the *CREBS* locus in H3.3K27M DIPG, with minimal toxicity towards normal cells. Moreover, the combination therapy of ABBV-075 and the BRG1 inhibitor shows promise in producing a synergistic therapeutic response in H3.3K27M DIPG patients.

**Discussion**

DIPG, a lethal pediatric cancer, is characterized by hyper-proliferation and differentiation arrest driven by H3K27M oncohistones. Our research uncovers an axis involving H3.3K27M oncohistone and *CREBS*/*ID1*, which sustains the stem-like state of DIPG cells. Specifically, we find that *CREBS* induces elevated *ID1* levels in the H3.3K27M subtype, promoting tumorigenesis; while BMP signaling regulates this process in the H3.1K27M subtype<sup>42,45–51</sup>. Furthermore, we demonstrate that H3.3K27M directly boosts *CREBS* expression by reshaping the H3K27me3 landscape at the *CREBS* locus, particularly at super-enhancer regions in DIPG cells. Additionally, we elucidate how *CREBS* collaborates with the SWI/SNF chromatin remodeling complex to drive oncogenic transcriptional changes in H3.3K27M DIPG. Intriguingly, disrupting *CREBS* super-enhancers with ABBV-075 significantly reduces its expression and inhibits H3.3K27M DIPG tumor growth. Lastly, combining ABBV-075 with a BRG1 inhibitor presents a promising therapeutic strategy for clinical translation in H3.3K27M DIPG treatment. These findings highlight the complexity of DIPG pathogenesis and underscore the significance of targeting oncogenic transcriptional networks for effective therapeutic intervention.

*ID1* is a master regulator for tumorigenesis in multiple cancers<sup>37,39,40,42</sup>. Previous work suggests that *ID1* is a downstream target of the BMP signaling pathway<sup>42,45</sup>. Our current study revealed that *ID1* functions as an oncogenic factor regardless of BMP signaling activity levels in H3K27M DIPG. Furthermore, we identified *CREBS* as an upstream regulator of *ID1* in the low BMP signaling activity subtype, operating independently of BMP signaling. Notably, *CREBS* functions as an oncogenic transcription factor essential for promoting proliferation and maintaining stemness in H3.3K27M-glioma cells. Given *CREBS*'s established role as an oncogenic factor in various cancer types<sup>29,30,36</sup>, further research into the *CREBS*/*ID1* axis is imperative to gain a comprehensive understanding of its mechanisms in tumorigenesis. This is



particularly essential for tumors exhibiting *ID1* higher expression within a context of low BMP signaling activity.

Approximately 80% of DIPG patients harbor K27M mutations in the genes encoding the histone variant H3.3, while only ~20% exhibit mutations in the histone variant H3.1<sup>6,7,10</sup>. The canonical histone H3.1 and the noncanonical histone H3.3 differ by five amino acids, and they

are incorporated into nucleosomes via replication-dependent and replication-independent mechanisms, respectively<sup>98,99</sup>. These amino acid differences are crucial as they mediate interactions with specific histone chaperones, influencing the choice of nucleosome assembly pathways<sup>100</sup>. Additionally, the H3.3 variant is characterized by a restricted genomic distribution, generally limited to regions of active

**Fig. 7 | Combinatorial approach with ABBV-075 and BRG1 inhibition shows synergistic effects for H3.3K27M DIPG treatment.** **a** Indicated DIPG cells were treated with JQ1 and ABBV-075 with a series of concentrations for 72 hours (left). Viability of indicated cells treated with JQ1 (300 nM) and ABBV-075 (60 nM) for the number of days indicated ( $n = 3$  independent experiments) (right). **b** Neural sphere formation and quantification of the TT150630, TT150714, and PPC cells treated with 0.1% DMSO, 300 nM JQ1, or 60 nM ABBV-075 for 10 days.  $N = 3$  independent experiments. Scale bars: 1 mm. **c, d** The bioluminescence activity (**c**) was plotted with representative bioluminescence images (**d**) and the statistical difference between saline and ABBV-075 treatment groups from animals implanted with TT150630 cells ( $n = 5$  mice in each group). **e** Kaplan-Meier analysis from animals implanted with TT150630 cells with saline or ABBV-075 treatment ( $n = 5$ ) in the

pons. **f** Cell viability matrix for DIPG17 and TT150714 DIPG cells treated with distinct ABBV-075 (y-axis) and BRM014 (x-axis) ranging from 0 to 1000 nmol/L ( $n = 3$  independent experiments). **g, h** The data obtained in **f** were used to calculate the combination index (CI) values using Chou-Talalay via CompuSyn (**g**) or Bliss synergy (**h**) analysis and showed in heatmap matrix (CI < 1, = 1, and > 1 indicates synergism, additive, and antagonism, respectively). Bliss score > 10 represents a strong synergism ( $n = 3$  independent experiments), representative heatmaps were shown in (**g**) and (**h**). Data presented as mean  $\pm$  s.e.m. of three independent experiments (**a** and **b**) or mean  $\pm$  s.e.m. (**c**), statistical significance was determined by a two-tailed unpaired Student's *t*-test (**a**, **b**, and **c**) or log-rank test (**e**). Experiments were repeated three times independently with similar results (**f** and **g**). Source data are provided as a Source Data file.

chromatin and gene bodies<sup>23</sup>, whereas the H3.1 variant is more diffusely distributed throughout the genome. Such distributional differences could contribute to distinct epigenomic conformations and cellular origins<sup>4</sup>.

Indeed, each variant of H3K27M in DIPG tends to acquire distinct secondary mutations: H3.3K27M commonly co-occurs with TP53 mutations, while H3.1K27M is frequently associated with ACVR1 mutations<sup>46–48</sup>. Previous studies have suggested that H3.1K27M oncohistones stall DIPG development at the OPC stage, facilitating the acquisition of oncogenic BMP signaling by progenitor cells. This process leads to phosphorylation of SMAD1/5/8 and upregulation of ID1 gene expression, thereby enhancing stemness and inhibiting senescence<sup>46–48</sup>. However, our studies indicate a different mechanism for the H3.3K27M oncohistone, which primes the epigenome of *CREB5*, subsequently upregulating ID1 expression and maintaining DIPG stemness. Notably, H3.1K27M oncohistones do not incorporate into the *CREB5* locus or regulate the *CREB5* epigenome.

Interestingly, recent research has demonstrated that DIPG tumors with H3.1K27M and H3.3K27M mutations display distinct active enhancer profiles. Our findings reveal that *CREB5* expression and its enhancer landscape are markedly lower in H3.1K27M tumors compared to H3.3K27M DIPG tumors. The differential effects of H3.1K27M and H3.3K27M on the epigenome appear to be significantly influenced by the progenitor cell state and identity. Both mutations uniformly restrict H3K27me3 deposition to PRC2 nucleation sites specific to the cell of origin, and the impaired propagation of this repressive mark may be central to their oncogenic potential<sup>4</sup>.

Targeting oncogenic transcription factors poses a significant challenge in cancer treatment due to their essential role in regulating gene expression programs that drive tumorigenesis<sup>101–103</sup>. Strategies have been proposed to address this challenge, including the design of specific protein degraders and the use of epigenetic inhibitors to modulate their expression<sup>103–105</sup>. Our study focuses on *CREB5*, a gene associated with super-enhancers and highly ranked in H3.3K27M DIPGs. Through our drug miniscreen, we found that ABBV-075 effectively reduces *CREB5* expression by disrupting the DNA accessibility of super-enhancers, even at low concentrations, while demonstrating potent activity against BRD4 and minimal impact on normal cells ( $K_d = 1$  nM; 90-fold selectivity vs JQ1)<sup>90</sup>. The successful Phase I clinical trial (NCT02391480, NCT04480086) of ABBV-075 in multiple cancers has validated its safety and efficacy<sup>91,106–108</sup>, paving the way for subsequent clinical translation in treating H3.3K27M DIPG.

Considering *CREB5*'s documented overexpression in various cancers beyond those included in ABBV-075 clinical trials<sup>29,30,36</sup>, it is worth investigating whether *CREB5* ranks among the top super-enhancer-associated genes in these cancers. If so, leveraging ABBV-075's anti-tumor efficacy could be beneficial in treating those cancers.

Our findings highlight the critical interplay between *CREB5* and the SWI/SNF chromatin remodeler complex, specifically implicating BRG1, a known dependency in H3K27M DMGs, in tumor progression<sup>27,87,95</sup>. Recent studies demonstrate that pharmacological

inhibition of BRG1 reduces DMG tumor growth in preclinical models<sup>27,87,95</sup>, aligning with our research and further validating the importance of *CREB5* and chromatin remodeling in DIPG pathogenesis. Notably, we show that combined inhibition of ABBV-075 and BRG1 may synergize as a therapeutic strategy for H3.3K27M DIPG. However, the combination therapy involving ABBV-075 and BRM-014 demonstrated antagonistic interactions at certain dose combinations, underscoring the importance of careful dose optimization. These findings underscore the potential of targeting oncogenic transcriptional networks to improve outcomes in aggressive pediatric brain tumors.

## Methods

### Ethics statement

Our research complies with all relevant ethical regulations of Tsinghua University. The animal experiments conducted as part of this research were completed under guidelines provided by the Institutional Animal Care and Use Committee (IACUC) of Tsinghua University. Mice were monitored weekly for signs of ill health or overt tumors. Once mice displayed signs of hydrocephalus (domed head) or neurological distress, they were killed humanely as defined by IACUC (17-XQR1, PI: Qiaoran Xi). IACUC guidelines recommend limiting solid tumors to 10% of the host's body weight. This criterion was not exceeded in this study. All human cell cultures were generated with written and/or signed informed consent from parents or legal adult representatives for pediatric patients, in compliance with the Institutional Review Board (IRB) of Beijing Tiantan Hospital under approved protocols (KY 2018-042-02). Written and/or signed informed consent was obtained from parents or legal adult representatives for pediatric patients. The consent includes permission to publish information that could potentially identify individuals in scientific publications or presentations.

### Plasmids

The sequences encoding wild-type and K27M-mutant forms of human H3.1 and H3.3 cDNA were generated by PCR amplification of human complementary DNA (cDNA) from PPC cells and DIPG cells, respectively. These were flanked by EcoRI and KpnI recombination sites and directly inserted into pCI vector fused with HA tag (N-terminal on insert) via IN-FUSION cloning.

### Cell lines and cell culture

Patient-derived H3K27M-glioma DIPG cell lines (TT150630, TT150714, TT150728, TT150210) and normal pontine progenitor cell (PPC) were kindly provided by Dr. Liwei Zhang. Briefly, DIPG cells were cultured in plates with Matrigel (cat. #356234, Corning) (1%, 4–12 h at 37 °C) and containing a serum-free medium with the following composition: DMEM (cat. #C11995500BT, Invitrogen), B27 (cat. #17504044, Gibco), N2 (cat. #17502048, Gibco), bFGF (20 ng mL<sup>-1</sup>; cat. #100-18B, PeproTech), EGF (20 ng mL<sup>-1</sup>; cat. #AF-100-15, PeproTech), PDGF-AB (20 ng mL<sup>-1</sup>; cat. #100-00AB, PeproTech) and 1%

penicillin/streptomycin (cat. #03-033-1B, Biological Industries). Previously characterized human fetal pontine progenitor cells (PPCs) were cultured in the above medium without PDGF-AB. HEK293T (cat. CRL-3216, ATCC) cells were grown in a DMEM medium supplemented with 10% FBS (cat. #FCS500, ExCell Bio) and 1% penicillin/streptomycin. SU-DIPGXVII cells (DIPG17) and SU-DIPGIV cells (DIPG-IV) were kindly provided by Y. Tang. These two cells were cultured in tumor stem media (TSM) base supplemented with 1x B27 supplement without vitamin A (cat. #12587001, Gibco), 1% penicillin/streptomycin (cat. #03-033-1B, Biological Industries), 1x GlutaMAX-I supplement (cat. #35050-060, Thermo Fisher), human growth factors (20 ng mL<sup>-1</sup> EGF, 20 ng mL<sup>-1</sup> bFGF, 10 ng mL<sup>-1</sup> PDGF-AA, cat. #100-13A, PeproTech, 10 ng mL<sup>-1</sup> PDGF-BB, cat. #AF100-14B-100, PeproTech) and heparin (2 µg mL<sup>-1</sup>; cat. #07980, StemCell Technologies). The brains of E11.5, E13.5, and E15.5 mouse embryos were dissected and separated into forebrain and hindbrain regions, distinguished by the expression of *Foxg1* and *Irx2*, respectively. Progenitor cells from both regions were mechanically dissociated and subsequently seeded onto Matrigel-coated 6-well plates (Excell Bio, CS016-0092) in Mouse NeuroCult Proliferation Medium (Stem Cell Technologies, 05702), supplemented with human EGF (20 ng/mL). The cells were dissociated for passaging using TrypLE Express Enzyme without phenol red (cat. #12604013, Gibco) for 3 to 5 minutes at 37 °C. Cells were passaged 1 to 6 times before being used in the described experiments. We confirmed the authenticity of all cells by analyzing short tandem repeats. Mycoplasma testing was regularly performed every 3 months and all cells were tested negative for the presence of mycoplasma.

All cells were grown in a humidified atmosphere with 5% CO<sub>2</sub> at 37 °C.

### Immunocompromised mice

The present xenograft animal study used for the 4-week-old female NOD/ShiLtJGpt-Prkdc<sup>em26Cd52</sup>Il2rg<sup>em26Cd22</sup>/Gpt (NCG mice) (GemPharmatech). Animals were housed at 20–22 °C with 12 h:12 h light: dark cycles at 50–60% humidity. This study is compliant with all of the relevant ethical regulations regarding animal research. Sex was not considered in the study design and analysis because previous research indicates that DIPG occurs with similar frequency and characteristics across both sexes and this study was not designed to detect sex differences. Only female mice were used for this study, and all mouse data were collected from female mice.

### Intracranial xenotransplantation

All experiments were performed using orthotopic cell xenograft models that were generated by injecting luciferase-engineered DIPG cells into the pons of 4-week-old female NCG mice. Specifically, DIPG cells were injected stereotactically into the right pons of 4-week-old female NCG mice treated with 0.05 mg/kg buprenorphine and anesthetized with 375 mg/kg Avertin. We resuspended 2 × 10<sup>5</sup> DIPG cells in 5 µL PBS and implanted them into the brainstem of immunodeficient mice at a rate of 0.5 µL/minute under the control of Nanoject III Programmable Nanoliter Injector (Drummond Scientific Company). Upon completing the injection, the needle was left in place for another minute and then withdrawn slowly to help reduce cell reflux. Mice were returned to their cages after closing the scalp with suture and staple, placed on a warming pad, and visually monitored until full recovery. Mice were then checked daily for signs of distress, including seizures, weight loss, and tremors, and euthanized as they developed neurologic symptoms, including head tilt, seizures, sudden weight loss, loss of balance, and/or ataxia. Tumor growth was monitored weekly for TT150630 and DIPG17 mice using the IVIS Spectrum In Vivo Imaging System (PerkinElmer), starting 7 days after cell injections. All animal studies were performed according to the Tsinghua University Institutional Animal Care and Use Committee (IACUC)-approved protocols (17-XQR1, PI: Qiaoran Xi).

### AAV injection by convection-enhanced delivery (CED)

Mice harboring pontine DIPG xenografts were treated with either AAV-ID1 KD or control at the tumor site by CED injection. Before the CED procedure, animals were injected subcutaneously with the analgesic buprenorphine (0.05 mg/kg) and then anesthetized with 375 mg/kg Avertin. After placing the animals on a stereotactic frame, the skull of the mouse was exposed through a small skin incision, and a small burr hole was made using a 25-gauge needle at lambda: -1.0 mm X, -0.8 mm Y, and 5.0 mm Z. The mice were injected with 5 µL AAV virus at a titration of 1–3 × 10<sup>11</sup> (molecules/µL) by infusion using an auto-injector at a 0.5 µL/min rate for a total amount of 1 × 10<sup>12</sup> of AAV-ID1 KD virus. Upon infusion, the needle was left in place for another 1–2 minutes and then withdrawn slowly to help reduce reflux. Animals were returned to their cages to recover and resumed normal active behavior within 3–12 hours.

### Viral production and generation of DIPG stable cell lines

We established DIPG cell lines containing luciferase-green fluorescent protein (GFP) by infecting the DIPG cells with pLEX-based lentivirus carrying luciferase-GFP. The lentivirus plasmid was kindly provided by H. Zheng. To generate plasmids containing short hairpins against *ID1*, *CREBS*, *SMADI*, and *H3F3A*, we digested the pLKO.1 vector with *EcoRI*/*AgeI* enzymes and then ligated it with the annealed oligos. We provide a list of the shRNA oligonucleotide pair sequences in the Supplementary Table 4.

Target plasmids, RRE, REV, and VSVG were co-transfected into HEK293T cells for lentivirus packaging using Lipofectamine 2000. The supernatants containing lentivirus particles were collected 48 h after transfection and then concentrated by 5x Lentivirus Concentration Reagent (cat. #C103-01, GenStar). For lentiviral infection, DIPG cells were incubated with shRNA expressing lentivirus for 48 h before being replaced with a fresh medium. The infected cells were selected with puromycin (cat. #p8833, Sigma) for further experiments.

**Cell viability assay.** We performed cell viability assays using the CellTiter-Blue Luminescent Cell Viability Assay (cat. #PR-G8081, Promega) according to the specifications available from the manufacturer. The cells were plated in 96-well plates (a seeding density of 3000 cells per well). The cells were incubated with CellTiter-Blue reagent for 3 hours, and luminosity intensity was measured every 2 days until day 6. To ensure statistical robustness, we performed at least three independent replicates of each condition and inferred significance using a two-tailed unpaired Student's *t*-test.

**Sphere formation assay.** The sphere formation assay was performed by seeding 3000 DIPG cells in each ultralow attachment 96 wells (cat. #3474, Corning) present in each plate. At least triplicates were performed for each condition. The cells were cultured for a total of 10 days, with an extra 20–30 µL medium being added to each well every other day. We used an Opera Phenix confocal microscope (Perkin Elmer) to obtain the Panoramic images for each condition.

**Cell cycle and apoptosis analysis.** Cell cycle analysis and apoptosis assay were performed using the Cell Cycle and Apoptosis Analysis Kit (cat. #C1052, Beyotime) staining. A total of 10<sup>6</sup> DIPG cells were washed with ice-cold PBS buffer twice. We then harvested the cells and stained them following the instructions of the manufacturer. We then performed FACS analysis to analyze the cell cycle and count the proportion of cells that underwent apoptosis. The original data were analyzed using FlowJo v.10 (FlowJo, LLC).

**In vitro limiting dilution assay.** The neurosphere formation capacity was assessed using a limiting dilution assay<sup>61</sup>. Cells were seeded at decreasing densities (100, 50, 20, 10, 5, 2 cells per well) into 96-well plates. After 7–12 days of incubation, the presence and number of neurospheres containing more than five cells per well were recorded.

Data analysis was performed using the software available at <http://bioinfo.wehi.edu.au/software/elda>.

**Bioluminescence imaging.** Mice were anesthetized with isoflurane before bulbus oculi injection. Imaging started 1 min after the injection of D-luciferin (cat. #40902ES01, Yeason). The bioluminescence signal was measured using the region of interest tool available in the Living Image v.4.4 software.

### Histopathology and immunohistochemistry

Histopathological evaluation of the mouse pontine was performed on H&E-stained paraffin sections. For H&E, we used xylene to deparaffinize 5  $\mu$ m-thick sections twice and for 3 min each time. The slides were then gradually and consecutively immersed for 3 min in 100%, 95%, 70%, and 50% ethanol. The slides were counterstained with H&E and dehydrated before adding the mounting medium. To perform immunohistochemistry staining, sections were deparaffinized with xylene, rehydrated, and finally subjected to antigen retrieval in a citrate-based buffer (cat. #ZLI-9064, ZSGB-BIO) in a microwave oven for 15 min. The slides were incubated with 3% H<sub>2</sub>O<sub>2</sub> for 10 min at room temperature and blocked with a solution containing PBS and 5% bovine serum albumin (cat. #V900933, Sigma) for 1 h before overnight incubation with OLIG2 (1:200, Millipore, cat. #AB9610) or GFAP (1:500, Dako, cat. #z0334) antibody. The slides were subsequently incubated with the secondary antibody conjugated with ImmPACT and then with ImmPACT DAB EqV Substrate (cat. #ZLI-9019, ZSGB-BIO). Finally, the slides were fixed in the mounting medium (cat. #S2100, Solarbio). The stained tissue samples were visualized on a Panoramic SCAN (3DHISTECH) microscope using a 40x objective. CaseViewer (v2.3, 3DHISTECH) software was used for analysis.

### Immunofluorescence

For the immunofluorescence, cells were seeded on a glass slide in the 6-well plate. The attached cells were fixed using 4% paraformaldehyde in PBS pH 7.4 for 15 min at room temperature (RT) with 60% cell confluency and then permeabilized for 10 min with PBS containing either 0.05% Triton X-100. Permeabilized cells were incubated with 2% BSA in PBS for 60 min to block non-specific absorption of the antibodies and then were incubated with the diluted primary antibody in 2% BSA in PBS overnight at 4 °C. Primary antibodies used were H3K9me2 (1:100, Active Motif, cat. #39683, clone MABI 0307) or human nuclear antigen (NHA) (1:200, Millipore, cat. #4383, clone 3E1.3). On the next day, the glass slide in the 6-well plate was first washed with PBS 3 times (5 min each) and then incubated with Alexa Fluor 594 secondary antibody (1:1000, Invitrogen, cat. #A-21207) for 1 hour at RT. After PBS washing 3 times (5 min each), we used 4,6-diamidino-2-phenylindole (DAPI) (1:10,000; cat #C0060, Solarbio) as a nuclear stainer. After another PBS washing 3 times (5 min each), the glass slide was mounted with a drop of ProLong™ Gold Antifade Mountant solution (cat. #P36930, Invitrogen), and observed the stained cells using an Olympus FV-3000 confocal microscope. For cryosections, fixed mouse brains were taken through a sucrose gradient, embedded in O.C.T (cat. #4583, Tissue-Tek), and sectioned at 15  $\mu$ m on a cryostat (cat. #CM3050S, Leica). Primary antibodies were OLIG2 (1:200, Millipore, cat. #AB9610) or GFAP (1:500, Dako, cat. #z0334). The secondary antibody was Alexa Fluor 594 secondary antibody (Invitrogen, cat. #A-21207). The number of OLIG2<sup>+</sup> or GFAP<sup>+</sup> cells within the field of view (FOV) was analyzed by Fiji ImageJ software (v1.43, Freeware/NIH).

### Western blotting

Cell lysates were prepared using RIPA lysis buffer (50 mM Tris-HCl pH8.0, 150 mM NaCl, 1% Triton X-100, 5 mM EDTA) together with phosphatase (cat. #B15001, Bimake) and protease (cat. #B14001, Bimake) inhibitor cocktails, followed by the measurement of protein

concentration using the Quantitative Protein Determinations Kit by BCA-assay (cat. #HX18651, huaxingbio). Extracted proteins were boiled at 100 °C for 10 min and then subjected to electrophoresis through 8-15% SDS-polyacrylamide gel electrophoresis.

### Immunoprecipitation and mass spectrometry

Whole cell lysates were prepared from exponentially growing cells. The cell pellets were obtained after centrifugation at 500 g for 5 min, and then lysed in whole cell lysis (WCL) buffer (50 mM Tris-HCl pH8.0, 150 mM NaCl, 1% Triton X-100, 5 mM EDTA) supplemented with protease inhibitors cocktail. Cell lysates were incubated on ice for 30 min and pulverized with ultrasonication for 1 min on ice, finally the lysates were cleared by centrifugation at 13,000 g for 10 min at 4 °C. The soluble supernatant was collected and incubated with Anti-Flag Affinity Gel (cat. #B23102, Biotool) overnight at 4 °C by gently mixing on a suitable shaker. Beads were then washed with WCL buffer for 4 times, and captured protein complexes were boiled in SDS sample buffer. The obtained samples were then loaded onto SDS-polyacrylamide gel electrophoresis (PAGE) and stained using Commassie blue staining solution, and all the bands were cut from the gel. The proteins were digested with trypsin at 37 °C overnight for 16 h. Tryptic peptides were desalted and labeled with the TMT 6-plex reagents. Then, the mixed labeled peptides were subjected to LC-MS/MS sequencing. Mass spectrometry analysis was performed using a Q Exactive Plus liquid mass spectrometry system (cat. #14017289, Thermo Scientific). The analytical column was a C-18 resin (5  $\mu$ m, 300 Å, Thermo Scientific) packed fused silica capillary column (150 mm length, 75  $\mu$ m inner-diameter, Thermo Scientific). The mass spectrometer was operated in the data-dependent acquisition (DDA) mode using Xcalibur (v4.1.31.9) software and MS1 spectra were obtained at a mass range of 300-1800 *m/z* with 60,000 resolution. The Automatic Gain Control (AGC) target was 3e and the spray voltage was 3800 V. As for MS2 analysis, the top 40 most intense precursor ions were fragmented in the HCD collision cell at 32% normalized collision energy using a 0.4 Da isolation window with a dynamic exclusion duration time of 15 s. Besides, the AGC target was 1e and the maximum injection time was 100 ms. The raw mass spectrometry data were searched by MaxQuant (v1.6.2.10) against an UniProtKB human database, and the database search algorithm used was MaxLFQ. The following parameters were used for database searching: static modifications of TMT 6-plex (or 10-plex) on lysine or carbamidomethylation (+57.021 Da) or N terminus (+229.130 Da) on cysteine; dynamic modification of oxidation (+15.995 Da) on methionine; the mass tolerances of precursors and fragments were 0.02 Da and 10 ppm, respectively; two missed cleavages were allowed; at least two unique peptides for quantification of proteins. Comparisons were made between different experimental groups (CREB5-Flag experiment group, *n* = 2; EV-Flag control group, *n* = 2; total number of samples analyzed is 4), and the quantitative difference ratio (ratio) was calculated for each protein. The proteins with significant differences between different experimental groups were screened according to the ratio. The logarithmic value of the ratio was taken as a base of 2, fitted to a normal distribution, and mean  $\pm 1.64$ \*SD was calculated. Finally, the identified proteins were inferred from the peptides against the human Uniprot using an FDR of 1%.

### Dual-luciferase reporter assay

For the luciferase reporter assay, *IDI* promoter region (chr20: 30191501-30193173), *CREB5* promoter region (chr7: 28448138-28450138), *CREB5* super-enhancer region (chr7:28725000-28727000), and *CREB5* typical enhancer region (chr7: 28771000-28773000) were cloned into pGL3-Basic vector. On the first day,  $1 \times 10^5$  293 T cells were seeded in 24-well plates. On the following day, 1000 ng luciferase reporter vector and 100 ng pCMV-Renilla vector were co-transfected with Lipofectamine 2000 (cat. #11668019, Thermo Fisher Scientific). Cells were harvested 48 hrs after transfection, and the luciferase

activities of lysed cells were assayed using the Dual Luciferase Reporter Gene Assay Kit (cat. #11402ES60, Yeason) on a multiple microplate luminometer (PerkinElmer EnVision). Firefly luciferase reporter activity was normalized to Renilla luciferase internal control.

### Compound efficacy assays

Cells were plated at a density of 5000 cells/well on Matrigel-coated 96-well plates, and cultured in the presence of ABBV-075, JQ1, BRM014, or other drugs with triplicate samples for each incubation condition. Drugs were combined by adding one compound in rows and another in columns with serial dilutions, resulting in a 5 × 5 dose matrix. Cell viability was assessed by the CellTiter-Blue luminescent cell viability assay. The combination index (CI) values were computed using Chou-Talalay via CompuSyn software. SynergyFinder (<https://synergyfinder.fimm.fi>) was used for interactive analysis and visualization of drug combination profiling data following the Bliss independence model.

### RNA-seq and qRT-PCR

Total RNA was extracted using a Total RNA Purification Kit according to the protocol made available by the manufacturer (cat. #8034111, DAKWE), and resuspended in 30 µL nuclease-free water. RNA libraries were prepared for sequencing using the Illumina TruSeq Stranded Total RNA Library Prep Kit. The libraries were sequenced on the Illumina HiSeq X platform (Novogen). A total of 1 µg purified RNA was reverse transcribed using the RevertAid First Strand cDNA Synthesis Kit (cat. #K1622, Thermo Fisher Scientific) following the manufacturer's specifications, and quantitative PCR was performed using SYBR Green (cat. #A311-10, GenStar) on a Viia7 Real-Time PCR system (Thermo Fisher Scientific). The primers are listed in the Supplementary Table 5. The experiments were performed in biological triplicates unless otherwise stated, and normalized to GAPDH as an internal control.

### Cleavage under targets & tagmentation (CUT&Tag) and sequencing

Cleavage under targets & tagmentation (CUT&Tag) were conducted in H3K27M KD and WT DIPG17 cells, CREB5 KD and WT DIPG17 cells, and H3K27M OE and WT PPC cells to profile H3K27me3, H3K27ac, H3K9me2, BRG1 or CREB5 chromatin association. 0.5 million cells were collected for CUT&Tag of H3K27me3, H3K27ac, H3K9me2, BRG1, or CREB5, and the DNA library was prepared through PCR according to the manufacturer's protocol (cat. #12598ES12, Yeason). The sequencing libraries were quantified and quality assessed with Qubit 2.0 and Agilent 2100. DNA fragments ranging from 200-600 bp were selected for PCR-assisted library using magnetic beads. For quantitative analysis, 5 pg E. coli λ DNA was added into the samples as DNA spike-in by exogenous reference genome normalization. Sequencing libraries were multiplexed and run on an Illumina HiSeq platform.

### Assay for Transposase-Accessible Chromatin using sequencing (ATAC-seq) library generation and sequencing

ATAC-seq experiments were conducted in CREB5 KD and WT DIPG17 cells to profile the DNA accessibility. 0.5 million cells were collected for ATAC-seq, and the DNA library was prepared through PCR using a commercial ATAC kit (cat. #N248, Novoprotein Inc.) according to the manufacturer's protocol. The sequencing libraries were qualified with Qubit 2.0 and Agilent 2100, and sequenced on an Illumina HiSeq platform for each library.

### CUT&RUN and sequencing

CUT&RUN was performed in DIPG17 cells. DIPG cells ( $5 \times 10^5$ ) were harvested for CUT&RUN of CREB5, and the DNA library was prepared through PCR using the manufacturer's protocol (cat. #HD102, Vazyme). The sequencing libraries were qualified with Qubit 2.0 and Agilent 2100, and sequenced on an Illumina HiSeq platform for each library.

### Bioinformatical analysis of RNA-seq, CUT&Tag, and ATAC-seq data

In general, GNU parallel was used to improve the analysis efficiency if possible. For RNA-seq analysis: Reads were quality checked with FastQC v0.11.5 and mapped to the human (hg19) genome with Bowtie2 v2.3.3 using standard settings for paired reads. The .sam and .bam files were manipulated with samtools v1.9. On average, 80% of reads were uniquely mapped. Uniquely mapped reads were assigned to annotated genes with featureCounts v2.0.1 using default settings. Read counts were then normalized by library size and differential gene expression analysis based on a negative binomial distribution was conducted with DESeq2 packages in R language. Unless otherwise indicated, the threshold for differential expression was set as follows: adjusted  $p$ -value < 0.05,  $\log_2$  (fold change) > 1 or < -1, and average normalized read count > 11. KEGG pathway and GO term analyses were performed using DAVID databases. For ATAC-seq and CUT&Tag analysis: Reads were quality checked with FastQC v0.11.5 and mapped to the human (hg19) genome with Bowtie2 v2.3.3 using standard settings for paired reads. The .sam and .bam files were manipulated with samtools v1.9. Peaks were called using macs2 v2.1.4 with the default setting. Visualization of detected peaks was performed using deeptools v3.4.5, and downstream analyses were performed using DiffBind v3.2.4. Specifically, DiffBind was used to identify differential peaks of H3K27me3 in H3K27M-overexpressing PPC cells and H3K27M-KD DIPG17 cells compared with control PPCs and DIPG17 cells, respectively. A total of 7858 and 4171 significantly differential sites in PPC cells and DIPG17 cells were identified, where gained or lost peaks were defined with the threshold of FDR < 0.05 and  $|\log_2$  Fold Change| > 1. Annotation of the called peaks was performed with ChIP-seeker in the R package. The motif analysis was performed using the *findMotifGenome.pl* program in the HOMER suite with default parameters. The coverage files of publicly available ChIP/ATAC-seq datasets were first generated using the *multiBigWigSummary* program in the deeptools suite prior to constructing the correlation heatmaps. Following recommendations in the deeptools suite, we used Spearman correlation analysis to compare different genome-wide ChIP/ATAC-seq datasets. The resulting correlation heatmaps were visualized using the *plotCorrelation* program of the deeptools suite with the following parameters: [plotCorrelation -in file.npz -corMethod spearman -skipZeros -whatToPlot heatmap].

### 4C-sequencing and bioinformatics analysis

For each sample, 2 million cells were cross-linked in 1% formaldehyde for 10 min at room temperature and quenched with glycine to a final concentration of 0.2 M. Cross-linked samples were rinsed once with PBS. Cells were lysed using a buffer containing 10 mM Tris-HCl (pH 7.5), 10 mM NaCl, 5 mM MgCl<sub>2</sub>, 0.1 mM EGTA and Protease Inhibitor Cocktail. NlaIII (cat. #R0125, NEB) was used as primary restriction enzyme, DpnII (cat. #R0543) was used as secondary restriction enzyme. 4C-seq libraries were prepared by sequential NlaIII and DpnII digestion and ligation of T4 DNA ligase covering the mouse *Hoxa* clusters. For each viewpoint, a total of 1 µg of each purified 4C-seq template was amplified using 16 individual PCR reactions with inverse primers including Illumina Universal adaptor sequences (*iHoxa9*\_Forward:AATGATACGGCGACCACCGAGATCTACACACTCTTCCCTACACGACGCTCTTCCGATCTAGGGA TGCATAGATTCATG,*iHoxa9*\_Reverse:CAAGCAGAAGACGGCATAACGAGA TGTGACTGGAGTTCAGACGTGTGCTCTTCCGATCTACAGTGTTCAGT ATTTTGG; *iHoxa13*\_Forward:AATGATACGGCGACCACCGAGATCTACAC ACTCTTCCCTACACGACGCTCTTCCGATCTCACACTTGCACAACCA GAAATGC,*iHoxa13*\_Reverse:CAAGCAGAAGACGGCATAACGAGATGTGAC TGGAGTTCAGACGTGTGCTCTTCCGATCTGGCGAGGCTCAGGCTTTT AT). 4C-sequencing reads were trimmed, aligned to mouse reference genome (mm10) using Bowtie2, and translated to restriction fragments using r3Cseq R packages. For plotting the data, fragments counts were normalized (reads per million) and smoothed with a running mean. The smoothed and normalized fragment counts were averaged among

the replicates of the same 4C library samples and visualized with igvR R packages. Significant chromatin interactions were identified with r3Cseq packages using default parameters and differential interactions between hindbrain and forebrain were identified with the DESeq2 packages ( $|\text{Log}_2 \text{ Fold Change}| > 1$  and  $\text{FDR} < 0.05$ ).

### Molecular docking experiments

The goal of molecular docking techniques is to predict the conformation of the BRD4 inhibitor (ABBV-075) within its target binding site on BRD4. Initial structures of BRD4 and ABBV-075 were obtained from the Protein Data Bank (PDB: 3MXF) and ChemSpider (ChemSpider ID: 58172612), respectively. The preparations entail removing alternative residue conformations, co-factors, and unwanted water molecules, and adding hydrogen atoms and atomic partial charges. Specific predocking steps, such as defining and calculating a grid, involve selecting a user-defined rectangular box as the search space, entirely encompassed using AutoDockTools1.5.7. Following these preparation steps, docking simulations are conducted using Vina. The resulting molecular docking poses are visualized using the PyMOL2 molecular visualization software.

### Single-cell RNA sequencing analysis

Normalized human expression data for H3K27M-mutant DIPGs<sup>25</sup> was obtained from GSE102130. We extracted 2259 malignant DIPG cells from the 2458 cells based on the cell ID annotated from the single-cell.broadinstitute.org website (see link below): [https://singlecell.broadinstitute.org/single\\_cell/study/SCP147/single-cell-analysis-in-pediatric-midline-gliomas-with-histone-h3k27m-mutation?cluster=tSNE&spatialGroups=-&annotation=Type--group-study&subsample=all#study-visualize](https://singlecell.broadinstitute.org/single_cell/study/SCP147/single-cell-analysis-in-pediatric-midline-gliomas-with-histone-h3k27m-mutation?cluster=tSNE&spatialGroups=-&annotation=Type--group-study&subsample=all#study-visualize). Tumor cells with an astrocytic differentiation (AC-like), oligodendrocytic differentiation (OC-like), and OPC-like program were determined using stemness- and lineage scores from previous study<sup>25</sup> and k-means clustering. To characterize underlying transcription factor activities in the malignant OPC-like DIPG cell subpopulation, the SCENIC package was used to identify gene regulatory modules (termed regulons) in malignant H3K27M glioma cells. For each cell subpopulation, a regulon specificity score (RSS) was computed to determine the highly expressed cell type-specific transcription factors across different cell subpopulations.

### Super-enhancer analysis

For each primary DIPG cell line or H3K27M-expressing PPCs, active enhancers were defined as H3K27ac peaks called in the cell greater than 2 kb from a RefSeq annotated TSS. Super-enhancer (SE) calls for each sample were determined using Rank Ordering of Super-Enhancer (ROSE) with the cell's active enhancer set and full-depth deduplicated bam files. SE-associated genes were determined by finding the nearest RefSeq TSS to each SE called with HOMER annotatedPeaks.pl and a custom RefSeq GTF file without miRNA or snoRNA. All SE-associated genes were then compared between clusters, and the rank of each gene was determined as the rank of its SE. For genes associated with more than one SE, the highest rank was used. If a gene was not associated with an SE, it was assigned a rank of the number of SEs called in the sample + 1.

### Statistics and reproducibility

The statistical analyses employed in each plot are either described in the figure legends or the corresponding Methods section. Briefly, the grouped data are presented as the mean  $\pm$  s.e.m. unless stated otherwise. Statistical significance between groups was determined using GraphPad Prism (v8.0) by two-tailed unpaired Student's *t*-test. Data with multiple independent experiments were analyzed by one-way ANOVA with the Tukey test to determine statistically significant effects. Data distribution was assumed to be normal but this was not formally tested. Survival analysis was performed using the Kaplan-

Meier method, and differences between the groups were calculated by the log-rank test (e.g. Supplementary Data 2). *P* values are indicated in the related figures. As above, all quantitative analyses are expressed as mean  $\pm$  s.e.m. of at least three biological replicates. No statistical method was used to predetermine sample size. For mouse studies, at least five mice were used, which is determined by experimental feasibility and sample availability to demonstrate certain results. For IHC and IF experiments, staining was performed on the entire cohort (minimum of  $n = 3$  biological samples) at the same time. No data were excluded from the analyses. If not stated otherwise, the experiments were not randomized, and the investigators were not blinded to allocation during experiments and outcome assessment. Image analysis was performed at the same time for each experiment.  $P < 0.05$  is considered statistically significant.

### Reporting summary

Further information on research design is available in the Nature Portfolio Reporting Summary linked to this article.

### Data availability

The RNA-seq, CUT&Tag, 4C-seq, and ATAC-seq data generated in this study have been deposited in the GEO database under accession code GSE250467. The human PPC cell lines' CUT&Tag data generated in this study have been deposited in the Genome Sequence Archive Human database under accession code HRA006376 with restricted access. The raw and processed sequencing data are publicly available. The HRA006376 dataset is publicly available under controlled access due to compliance with the regulations set by the Ministry of Science and Technology of the People's Republic of China. Researchers may access the data by submitting a request through the Genome Sequence Archive Human database under accession number HRA006376 at <https://ngdc.cnbc.ac.cn/gsa-human/browse/HRA006376>. Access to the data requires institutional approval, completion of ethic training, and agreement to a Data Access Committee (DAC), as outlined at [https://ngdc.cnbc.ac.cn/gsa-human/document/GSA-Human\\_Request\\_Guide\\_for\\_Users\\_us.pdf](https://ngdc.cnbc.ac.cn/gsa-human/document/GSA-Human_Request_Guide_for_Users_us.pdf). Requests are typically processed within 1-2 weeks of submission. Once granted, access to the data will remain available for a period of 2 years. The protein mass spectrometry raw data generated in this study have been deposited in the ProteomeXchange database via the PRIDE partner repository under accession codes PXD053094 and PXD060271. The previously published microarray, bulk RNA-seq, scRNA-seq, ChIP-seq and ATAC-seq data used in this study that were reanalyzed here are available in the GEO database under accession codes numbers GSE50021, GSE154267, GSE108364, GSE185280, GSE162976, GSE78801, GSE158447, and GSE102130. Images in Figs. 3g, 6c, and Supplementary Figs. 6h, 9c were created in BioRender.com [<https://biorender.com>] under Academic License Terms with agreement numbers IO27UDPSWH and AC27UYRUND. The remaining data are available within the Article, Supplementary Information or Source Data file. Source data are provided with this paper.

### References

1. Jones, C. & Baker, S. J. Unique genetic and epigenetic mechanisms driving paediatric diffuse high-grade glioma. *Nat. Rev. Cancer* **14**, 651–661 (2014).
2. Mackay, A. et al. Integrated Molecular Meta-Analysis of 1,000 Pediatric High-Grade and Diffuse Intrinsic Pontine Glioma. *Cancer Cell* **32**, 520–537.e525 (2017).
3. Bjerke, L. et al. Histone H3.3 Mutations Drive Pediatric Glioblastoma through Upregulation of MYCN. *Cancer Discov.* **3**, 512–519 (2013).
4. Anastas, J. N. et al. Re-programming Chromatin with a Bifunctional LSD1/HDAC Inhibitor Induces Therapeutic Differentiation in DIPG. *Cancer Cell* **36**, 528–544.e510 (2019).

5. Srikanthan, D. et al. Diffuse intrinsic pontine glioma: current insights and future directions. *Chin. Neurosurg. J.* **7**, 6 (2021).
6. Wu, G. et al. Somatic histone H3 alterations in pediatric diffuse intrinsic pontine gliomas and non-brainstem glioblastomas. *Nat. Genet.* **44**, 251–253 (2012).
7. Schwartzentruber, J. et al. Driver mutations in histone H3.3 and chromatin remodelling genes in paediatric glioblastoma. *Nature* **482**, 226–231 (2012).
8. Lewis, P. W. et al. Inhibition of PRC2 Activity by a Gain-of-Function H3 Mutation Found in Pediatric Glioblastoma. *Science* **340**, 857–861 (2013).
9. Chan, K.-M. et al. The histone H3.3K27M mutation in pediatric glioma reprograms H3K27 methylation and gene expression. *Genes Dev.* **27**, 985–990 (2013).
10. Bender, S. et al. Reduced H3K27me3 and DNA Hypomethylation Are Major Drivers of Gene Expression in K27M Mutant Pediatric High-Grade Gliomas. *Cancer Cell* **24**, 660–672 (2013).
11. Harutyunyan, A. S. et al. H3K27M induces defective chromatin spread of PRC2-mediated repressive H3K27me2/me3 and is essential for glioma tumorigenesis. *Nat. Commun.* **10**, 1262 (2019).
12. Jain, S. U. et al. H3 K27M and EZHIP Impede H3K27-Methylation Spreading by Inhibiting Allosterically Stimulated PRC2. *Mol. Cell* **80**, 726–735.e727 (2020).
13. Oksuz, O. et al. Capturing the Onset of PRC2-Mediated Repressive Domain Formation. *Mol. Cell* **70**, 1149–1162.e1145 (2018).
14. Kraft, K. et al. Polycomb-mediated genome architecture enables long-range spreading of H3K27 methylation. *Proc. Natl Acad. Sci. USA* **119**, e2201883119 (2022).
15. Krug, B. et al. Pervasive H3K27 Acetylation Leads to ERV Expression and a Therapeutic Vulnerability in H3K27M Gliomas. *Cancer Cell* **35**, 782–797.e788 (2019).
16. Harutyunyan, A. S. et al. H3K27M in Gliomas Causes a One-Step Decrease in H3K27 Methylation and Reduced Spreading within the Constraints of H3K36 Methylation. *Cell Rep.* **33**, 108390 (2020).
17. Jessa, S. et al. K27M in canonical and noncanonical H3 variants occurs in distinct oligodendroglial cell lineages in brain midline gliomas. *Nat. Genet.* **54**, 1865–1880 (2022).
18. Andrade, A. F., Chen, C. C. L. & Jabado, N. Oncohistones in brain tumors: the soil and seed. *Trends Cancer* **9**, 444–455 (2023).
19. Piunti, A. et al. Therapeutic targeting of polycomb and BET bromodomain proteins in diffuse intrinsic pontine gliomas. *Nat. Med.* **23**, 493–500 (2017).
20. Piunti, A. & Shilatifard, A. The roles of Polycomb repressive complexes in mammalian development and cancer. *Nat. Rev. Mol. Cell Biol.* **22**, 326–345 (2021).
21. Mohammad, F. & Helin, K. Oncohistones: drivers of pediatric cancers. *Genes Dev.* **31**, 2313–2324 (2017).
22. Mohammad, F. et al. EZH2 is a potential therapeutic target for H3K27M-mutant pediatric gliomas. *Nat. Med.* **23**, 483–492 (2017).
23. Nagaraja, S. et al. Histone Variant and Cell Context Determine H3K27M Reprogramming of the Enhancer Landscape and Oncogenic State. *Mol. Cell* **76**, 965–980.e912 (2019).
24. Wang, J. et al. Epigenomic landscape and 3D genome structure in pediatric high-grade glioma. *Sci. Adv.* **7**, eabg4126 (2021).
25. Filbin, M. G. et al. Developmental and oncogenic programs in H3K27M gliomas dissected by single-cell RNA-seq. *Science* **360**, 331–335 (2018).
26. Jessa, S. et al. Stalled developmental programs at the root of pediatric brain tumors. *Nat. Genet.* **51**, 1702–1713 (2019).
27. Panditharatna, E. et al. BAF Complex Maintains Glioma Stem Cells in Pediatric H3K27M Glioma. *Cancer Discov.* **12**, 2880–2905 (2022).
28. Nomura, N. et al. Isolation and characterization of a novel member of the gene family encoding the cAMP response element-binding protein CRE-BP1. *J. Biol. Chem.* **268**, 4259–4266 (1993).
29. Wang, S. et al. CREB5 promotes invasiveness and metastasis in colorectal cancer by directly activating MET. *J. Exp. Clin. Cancer Res.* **39**, 168 (2020).
30. Hwang, J. H. et al. CREB5 Promotes Resistance to Androgen-Receptor Antagonists and Androgen Deprivation in Prostate Cancer. *Cell Rep.* **29**, 2355–2370.e2356 (2019).
31. Zhang, C.-H. et al. Creb5 coordinates synovial joint formation with the genesis of articular cartilage. *Nat. Commun.* **13**, 7295 (2022).
32. Feng, J. et al. TGF- $\beta$  signaling and Creb5 cooperatively regulate Fgf18 to control pharyngeal muscle development. *eLife* **11**, e80405 (2022).
33. Liu, X. et al. Single-cell RNA transcriptomic analysis identifies Creb5 and CD11b-DCs as regulator of asthma exacerbations. *Mucosal Immunol.* **15**, 1363–1374 (2022).
34. Kumar, A. et al. 2-Deoxyglucose drives plasticity via an adaptive ER stress-ATF4 pathway and elicits stroke recovery and Alzheimer's resilience. *Neuron* **111**, 2831–2846.e2810 (2023).
35. Wang, R. et al. CREB5 hypermethylation involved in the ganglioside GM1 therapy of Parkinson's disease. *Front Aging Neurosci.* **15**, 1122647 (2023).
36. Hwang, J. H. et al. CREB5 reprograms FOXA1 nuclear interactions to promote resistance to androgen receptor-targeting therapies. *eLife* **11**, e73223 (2022).
37. Sachdeva, R. et al. ID1 Is Critical for Tumorigenesis and Regulates Chemoresistance in Glioblastoma. *Cancer Res* **79**, 4057 (2019).
38. Jin, X. et al. The ID1-CULLIN3 Axis Regulates Intracellular SHH and WNT Signaling in Glioblastoma Stem Cells. *Cell Rep.* **16**, 1629–1641 (2016).
39. Anido, J. et al. TGF- $\beta$  Receptor Inhibitors Target the CD44<sup>high</sup>/Id1<sup>high</sup> Glioma-Initiating Cell Population in Human Glioblastoma. *Cancer Cell* **18**, 655–668 (2010).
40. Lasorella, A., Benezra, R. & Iavarone, A. The ID proteins: master regulators of cancer stem cells and tumour aggressiveness. *Nat. Rev. Cancer* **14**, 77–91 (2014).
41. Benezra, R., Davis, R. L., Lockshon, D., Turner, D. L. & Weintraub, H. The protein Id: A negative regulator of helix-loop-helix DNA binding proteins. *Cell* **61**, 49–59 (1990).
42. Huang, Y.-H. et al. ID1 Mediates Escape from TGF $\beta$  Tumor Suppression in Pancreatic Cancer. *Cancer Discov.* **10**, 142–157 (2020).
43. Perk, J., Iavarone, A. & Benezra, R. Id family of helix-loop-helix proteins in cancer. *Nat. Rev. Cancer* **5**, 603–614 (2005).
44. Massari, M. E. & Murre, C. Helix-Loop-Helix Proteins: Regulators of Transcription in Eucaryotic Organisms. *Mol. Cell. Biol.* **20**, 429–440 (2000).
45. Korchynskiy, O. & ten Dijke, P. Identification and Functional Characterization of Distinct Critically Important Bone Morphogenetic Protein-specific Response Elements in the Id1 Promoter\*. *J. Biol. Chem.* **277**, 4883–4891 (2002).
46. Taylor, K. R. et al. Recurrent activating ACVR1 mutations in diffuse intrinsic pontine glioma. *Nat. Genet.* **46**, 457–461 (2014).
47. Fontebasso, A. M. et al. Recurrent somatic mutations in ACVR1 in pediatric midline high-grade astrocytoma. *Nat. Genet.* **46**, 462–466 (2014).
48. Buczkowicz, P. et al. Genomic analysis of diffuse intrinsic pontine gliomas identifies three molecular subgroups and recurrent activating ACVR1 mutations. *Nat. Genet.* **46**, 451–456 (2014).
49. Fortin, J. et al. Mutant ACVR1 Arrests Glial Cell Differentiation to Drive Tumorigenesis in Pediatric Gliomas. *Cancer Cell* **37**, 308–323.e312 (2020).
50. Hoeman, C. M. et al. ACVR1 R206H cooperates with H3.1K27M in promoting diffuse intrinsic pontine glioma pathogenesis. *Nat. Commun.* **10**, 1023 (2019).
51. Carvalho, D. et al. ALK2 inhibitors display beneficial effects in preclinical models of ACVR1 mutant diffuse intrinsic pontine glioma. *Commun. Biol.* **2**, 156 (2019).

52. Sun, Y. et al. Context-dependent tumor-suppressive BMP signaling in diffuse intrinsic pontine glioma regulates stemness through epigenetic regulation of CXXC5. *Nat. Cancer* **3**, 1105–1122 (2022).
53. Messinger, D. et al. Therapeutic targeting of prenatal pontine ID1 signaling in diffuse midline glioma. *Neuro Oncol.* **25**, 54–67 (2023).
54. Sun, Y. et al. Potent anti-tumor efficacy of palbociclib in treatment-naïve H3.3K27M-mutant diffuse intrinsic pontine glioma. *EBioMedicine* **43**, 171–179 (2019).
55. Nagaraja, S. et al. Transcriptional Dependencies in Diffuse Intrinsic Pontine Glioma. *Cancer Cell* **31**, 635–652.e636 (2017).
56. Aibar, S. et al. SCENIC: single-cell regulatory network inference and clustering. *Nat. Methods* **14**, 1083–1086 (2017).
57. Van de Sande, B. et al. A scalable SCENIC workflow for single-cell gene regulatory network analysis. *Nat. Protoc.* **15**, 2247–2276 (2020).
58. Puget, S. et al. Mesenchymal transition and PDGFRA amplification/mutation are key distinct oncogenic events in pediatric diffuse intrinsic pontine gliomas. *PLoS One* **7**, e30313 (2012).
59. Chen, L. H. et al. The integrated genomic and epigenomic landscape of brainstem glioma. *Nat. Commun.* **11**, 3077 (2020).
60. Berlow, N. E. et al. IL-13 receptors as possible therapeutic targets in diffuse intrinsic pontine glioma. *PLoS One* **13**, e0193565 (2018).
61. Funato, K., Major, T., Lewis, P. W., Allis, C. D. & Tabar, V. Use of human embryonic stem cells to model pediatric gliomas with H3.3K27M histone mutation. *Science* **346**, 1529–1533 (2014).
62. Larson, J. D. et al. Histone H3.3 K27M Accelerates Spontaneous Brainstem Glioma and Drives Restricted Changes in Bivalent Gene Expression. *Cancer Cell* **35**, 140–155.e147 (2019).
63. Brien, G. L. et al. Simultaneous disruption of PRC2 and enhancer function underlies histone H3.3-K27M oncogenic activity in human hindbrain neural stem cells. *Nat. Genet.* **53**, 1221–1232 (2021).
64. Dunham, I. et al. An integrated encyclopedia of DNA elements in the human genome. *Nature* **489**, 57–74 (2012).
65. Eze, U. C., Bhaduri, A., Haeussler, M., Nowakowski, T. J. & Kriegstein, A. R. Single-cell atlas of early human brain development highlights heterogeneity of human neuroepithelial cells and early radial glia. *Nat. Neurosci.* **24**, 584–594 (2021).
66. Bhaduri, A. et al. An atlas of cortical arealization identifies dynamic molecular signatures. *Nature* **598**, 200–204 (2021).
67. Weng, Q. et al. Single-Cell Transcriptomics Uncovers Glial Progenitor Diversity and Cell Fate Determinants during Development and Gliomagenesis. *Cell Stem Cell* **24**, 707–723.e708 (2019).
68. Jiang, F. et al. Simultaneous profiling of spatial gene expression and chromatin accessibility during mouse brain development. *Nat. Methods* **20**, 1048–1057 (2023).
69. Miller, F. D. & Gauthier, A. S. Timing Is Everything: Making Neurons versus Glia in the Developing Cortex. *Neuron* **54**, 357–369 (2007).
70. La Manno, G. et al. Molecular architecture of the developing mouse brain. *Nature* **596**, 92–96 (2021).
71. Lee, A. P., Koh, E. G. L., Tay, A., Brenner, S. & Venkatesh, B. Highly conserved syntenic blocks at the vertebrate Hox loci and conserved regulatory elements within and outside Hox gene clusters. *Proc. Natl Acad. Sci.* **103**, 6994–6999 (2006).
72. Lehoczky, J. A., Williams, M. E. & Innis, J. W. Conserved expression domains for genes upstream and within the HoxA and HoxD clusters suggests a long-range enhancer existed before cluster duplication. *Evol. Dev.* **6**, 423–430 (2004).
73. Vieux-Rochas, M., Fabre, P. J., Leleu, M., Duboule, D. & Noordermeer, D. Clustering of mammalian Hox genes with other H3K27me3 targets within an active nuclear domain. *Proc. Natl Acad. Sci. USA* **112**, 4672–4677 (2015).
74. Ogiyama, Y., Schuettengruber, B., Papadopoulos, G. L., Chang, J. M. & Cavalli, G. Polycomb-Dependent Chromatin Looping Contributes to Gene Silencing during Drosophila Development. *Mol. Cell* **71**, 73–88.e75 (2018).
75. Eagen, K. P., Aiden, E. L. & Kornberg, R. D. Polycomb-mediated chromatin loops revealed by a subkilobase-resolution chromatin interaction map. *Proc. Natl Acad. Sci. USA* **114**, 8764–8769 (2017).
76. Gentile, C. et al. PRC2-Associated Chromatin Contacts in the Developing Limb Reveal a Possible Mechanism for the Atypical Role of PRC2 in HoxA Gene Expression. *Dev. Cell* **50**, 184–196.e184 (2019).
77. Liang, Z. et al. PICKLE-mediated nucleosome condensing drives H3K27me3 spreading for the inheritance of Polycomb memory during differentiation. *Mol. Cell* **84**, 3438–3454.e3438 (2024).
78. Hansen, K. H. et al. A model for transmission of the H3K27me3 epigenetic mark. *Nat. Cell Biol.* **10**, 1291–1300 (2008).
79. Margueron, R. et al. Role of the polycomb protein EED in the propagation of repressive histone marks. *Nature* **461**, 762–767 (2009).
80. Poepsel, S., Kasinath, V. & Nogales, E. Cryo-EM structures of PRC2 simultaneously engaged with two functionally distinct nucleosomes. *Nat. Struct. Mol. Biol.* **25**, 154–162 (2018).
81. De, S., Cheng, Y., Sun, M.-a, Gehred, N. D. & Kassis, J. A. Structure and function of an ectopic Polycomb chromatin domain. *Sci. Adv.* **5**, eaau9739 (2019).
82. Blackledge, N. P. & Klose, R. J. The molecular principles of gene regulation by Polycomb repressive complexes. *Nat. Rev. Mol. Cell Biol.* **22**, 815–833 (2021).
83. Furth, N. et al. H3-K27M-mutant nucleosomes interact with MLL1 to shape the glioma epigenetic landscape. *Cell Rep.* **39**, 110836 (2022).
84. Balsalobre, A. & Drouin, J. Pioneer factors as master regulators of the epigenome and cell fate. *Nat. Rev. Mol. Cell Biol.* **23**, 449–464 (2022).
85. Watt, A. C. et al. CDK4/6 inhibition reprograms the breast cancer enhancer landscape by stimulating AP-1 transcriptional activity. *Nat. Cancer* **2**, 34–48 (2021).
86. Kent, L. N. & Leone, G. The broken cycle: E2F dysfunction in cancer. *Nat. Rev. Cancer* **19**, 326–338 (2019).
87. Mo, Y. et al. Epigenome Programming by H3.3K27M Mutation Creates a Dependence of Pediatric Glioma on SMARCA4. *Cancer Discov.* **12**, 2906–2929 (2022).
88. He, Z., Chen, K., Ye, Y. & Chen, Z. Structure of the SWI/SNF complex bound to the nucleosome and insights into the functional modularity. *Cell Discov.* **7**, 28 (2021).
89. Lovén, J. et al. Selective Inhibition of Tumor Oncogenes by Disruption of Super-Enhancers. *Cell* **153**, 320–334 (2013).
90. McDaniel, K. F. et al. Discovery of N-(4-(2,4-Difluorophenoxy)-3-(6-methyl-7-oxo-6,7-dihydro-1H-pyrrolo[2,3-c]pyridin-4-yl)phenyl) ethanesulfonamide (ABBV-075/Mivebresib), a Potent and Orally Available Bromodomain and Extraterminal Domain (BET) Family Bromodomain Inhibitor. *J. Med. Chem.* **60**, 8369–8384 (2017).
91. Faivre, E. J. et al. Selective inhibition of the BD2 bromodomain of BET proteins in prostate cancer. *Nature* **578**, 306–310 (2020).
92. Moyer, M. W. First drugs found to inhibit elusive cancer target. *Nat. Med.* **17**, 1325 (2011).
93. Zuber, J. et al. RNAi screen identifies Brd4 as a therapeutic target in acute myeloid leukaemia. *Nature* **478**, 524–528 (2011).
94. Korb, E., Herre, M., Zucker-Scharff, I., Darnell, R. B. & Allis, C. D. BET protein Brd4 activates transcription in neurons and BET inhibitor Jq1 blocks memory in mice. *Nat. Neurosci.* **18**, 1464–1473 (2015).
95. Mota, M. et al. Targeting SWI/SNF ATPases in H3.3K27M diffuse intrinsic pontine gliomas. *Proc. Natl Acad. Sci.* **120**, e2221175120 (2023).
96. Chou, T.-C. & Talalay, P. Quantitative analysis of dose-effect relationships: the combined effects of multiple drugs or enzyme inhibitors. *Adv. Enzym. Regul.* **22**, 27–55 (1984).

97. Ianevski, A., Giri, A. K. & Aittokallio, T. SynergyFinder 2.0: visual analytics of multi-drug combination synergies. *Nucleic Acids Res.* **48**, W488–W493 (2020).
98. Burgess, R. J. & Zhang, Z. Histone chaperones in nucleosome assembly and human disease. *Nat. Struct. Mol. Biol.* **20**, 14–22 (2013).
99. Talbert, P. B. & Henikoff, S. Histone variants — ancient wrap artists of the epigenome. *Nat. Rev. Mol. Cell Biol.* **11**, 264–275 (2010).
100. Zhang, X. & Zhang, Z. Oncohistone Mutations in Diffuse Intrinsic Pontine Glioma. *Trends Cancer* **5**, 799–808 (2019).
101. Lee, T. I. & Young, R. A. Transcriptional regulation and its misregulation in disease. *Cell* **152**, 1237–1251 (2013).
102. Darnell, J. E. Transcription factors as targets for cancer therapy. *Nat. Rev. Cancer* **2**, 740–749 (2002).
103. Bushweller, J. H. Targeting transcription factors in cancer — from undruggable to reality. *Nat. Rev. Cancer* **19**, 611–624 (2019).
104. Heppler, L. N. & Frank, D. A. Targeting Oncogenic Transcription Factors: Therapeutic Implications of Endogenous STAT Inhibitors. *Trends Cancer* **3**, 816–827 (2017).
105. Bhagwat, A. S. & Vakoc, C. R. Targeting Transcription Factors in Cancer. *Trends Cancer* **1**, 53–65 (2015).
106. Faivre, E. J. et al. Exploitation of Castration-Resistant Prostate Cancer Transcription Factor Dependencies by the Novel BET Inhibitor ABBV-075. *Mol. Cancer Res.* **15**, 35–44 (2017).
107. Bui, M. H. et al. Preclinical Characterization of BET Family Bromodomain Inhibitor ABBV-075 Suggests Combination Therapeutic Strategies. *Cancer Res.* **77**, 2976–2989 (2017).
108. Piha-Paul, S. A. et al. First-in-Human Study of Mivebresib (ABBV-075), an Oral Pan-Inhibitor of Bromodomain and Extra Terminal Proteins, in Patients with Relapsed/Refractory Solid Tumors. *Clin. Cancer Res.* **25**, 6309–6319 (2019).
- (81872048). Y. T. is supported by National Natural Science Foundation of China (81972646, 82293661), Shanghai Frontiers Science Center of Cellular Homeostasis and Human Diseases, Innovative Research Team of High-Level Local Universities in Shanghai (SHSMU-ZDCX20212700).

### Author contributions

W.Z. and Q.X. initiated and designed the study; W.Z. performed the experiments; C.X., C.P., Z.J., L.X., and L.Z. provided the biopsy samples and clinical data of DIPG patients from Tiantan Hospital (Beijing); Y.T. provided DIPG17 and DIPG-IV cell lines; H. Q., X. L., and D. M. provided prenatal mouse brain slices. S.Y. and H.L. helped with western blot assay and animal experiments. W.Z. performed RNA-seq, 4C-seq, ATAC-seq, and CUT&Tag experiments; W. Z. did the bioinformatic analysis; all authors contributed ideas to the project. Q.X. supervised the project; W.Z. and Q.X. wrote the manuscript; all authors discussed the results and commented on the manuscript.

### Competing interests

The authors declare no competing interests.

### Additional information

**Supplementary information** The online version contains supplementary material available at <https://doi.org/10.1038/s41467-025-58795-2>.

**Correspondence** and requests for materials should be addressed to Liwei Zhang or Qiaoran Xi.

**Peer review information** *Nature Communications* thanks the anonymous, reviewers for their contribution to the peer review of this work. A peer review file is available.

**Reprints and permissions information** is available at <http://www.nature.com/reprints>

**Publisher's note** Springer Nature remains neutral with regard to jurisdictional claims in published maps and institutional affiliations.

**Open Access** This article is licensed under a Creative Commons Attribution-NonCommercial-NoDerivatives 4.0 International License, which permits any non-commercial use, sharing, distribution and reproduction in any medium or format, as long as you give appropriate credit to the original author(s) and the source, provide a link to the Creative Commons licence, and indicate if you modified the licensed material. You do not have permission under this licence to share adapted material derived from this article or parts of it. The images or other third party material in this article are included in the article's Creative Commons licence, unless indicated otherwise in a credit line to the material. If material is not included in the article's Creative Commons licence and your intended use is not permitted by statutory regulation or exceeds the permitted use, you will need to obtain permission directly from the copyright holder. To view a copy of this licence, visit <http://creativecommons.org/licenses/by-nc-nd/4.0/>.

© The Author(s) 2025

### Acknowledgements

We thank all the patients and families for donating tissues for this research. We are grateful to J. Massagué (Memorial Sloan Kettering Cancer Center), X. Jin and Y. Zou (Westlake University), C. David, H. Basnet, W. Xie, Z. Chen, H. Zheng, and W. Wu (Tsinghua University) for valuable discussions and critical readings of the paper; to H. Zheng for the luciferase-GFP plasmid; to R. Sun from the Laboratory Animal Research Center (Tsinghua University) for technical assistance with histological analyses and immunohistochemistry experiments; to J. Li and XL. Tian from the Protein Chemistry Facility for mass spectrometry analysis; to H. Zhang from the State Key Laboratory of Membrane Biology for flow-cytometry analysis; to D. Noordermeer (Université Paris-Saclay) and D. Duboule (University of Geneva) for their invaluable assistance on HoxA 4C data; and to staff of the Laboratory Animal Research Center for animal experiments during the COVID-19 pandemic. We thank the Tsinghua University Branch of China National Center for Protein Sciences (Beijing) for computational facility support. Images were created with GraphPad Prism 8. Q.X. is supported by National Key R&D Program of China (2022YFA1302704) and Tsinghua-Peking Center for Life Sciences. L.Z. is supported by Beijing municipal administration of Hospitals Clinical Medicine Development of Special Funding Support (ZYLX201608), Beijing Municipal Natural Science Foundation (7161004) and National Natural Science Foundation of China